Physics

Physics Research Publications

Purdue University *Year* 2010

Measurement of the top quark mass in the dilepton channel using m(T2) at CDF

T. Aaltonen, J. Adelman, B. A. Gonzalez, S. Amerio, D. Amidei, A. Anastassov, A. Annovi, J. Antos, G. Apollinari, A. Apresyan, T. Arisawa, A. Artikov, J. Asaadi, W. Ashmanskas, A. Attal, A. Aurisano, F. Azfar, W. Badgett, A. Barbaro-Galtieri, V. E. Barnes, B. A. Barnett, P. Barria, P. Bartos, G. Bauer, P. H. Beauchemin, F. Bedeschi, D. Beecher, S. Behari, G. Bellettini, J. Bellinger, D. Benjamin, A. Beretvas, A. Bhatti, M. Binkley, D. Bisello, I. Bizjak, R. E. Blair, C. Blocker, B. Blumenfeld, A. Bocci, A. Bodek, V. Boisvert, D. Bortoletto, J. Boudreau, A. Boveia, B. Brau, A. Bridgeman, L. Brigliadori, C. Bromberg, E. Brubaker, J. Budagov, H. S. Budd, S. Budd, K. Burkett, G. Busetto, P. Bussey, A. Buzatu, K. L. Byrum, S. Cabrera, C. Calancha, S. Camarda, M. Campanelli, M. Campbell, F. Canelli, A. Canepa, B. Carls, D. Carlsmith, R. Carosi, S. Carrillo, S. Carron, B. Casal, M. Casarsa, A. Castro, P. Catastini, D. Cauz, V. Cavaliere, M. Cavalli-Sforza, A. Cerri, L. Cerrito, S. H. Chang, Y. C. Chen, M. Chertok, G. Chiarelli, G. Chlachidze, F. Chlebana, K. Cho, D. Chokheli, J. P. Chou, G. Choudalakis, K. Chung, W. H. Chung, Y. S. Chung, T. Chwalek, C. I. Ciobanu, M. A. Ciocci, A. Clark, D. Clark, G. Compostella, M. E. Convery, J. Conway, M. Corbo, M. Cordelli, C. A. Cox, D. J. Cox, F. Crescioli, C. C. Almenar, J. Cuevas, R. Culbertson, J. C. Cully, D. Dagenhart, M. Datta, T. Davies, P. de Barbaro, S. De Cecco, A. Deisher, G. De Lorenzo, M. Dell'Orso, C. Deluca, L. Demortier, J. Deng, M. Deninno, M. d'Errico, A. Di Canto, G. P. di Giovanni, B. Di Ruzza, J. R. Dittmann, M. D'Onofrio, S. Donati, P. Dong, T. Dorigo, S. Dube, K. Ebina, A. Elagin, R. Erbacher, D. Errede, S. Errede, N. Ershaidat, R. Eusebi, H. C. Fang, S. Farrington, W. T. Fedorko, R. G. Feild, M. Feindt, J. P. Fernandez, C. Ferrazza, R. Field, G. Flanagan, R. Forrest, M. J. Frank, M. Franklin, J. C. Freeman, I. Furic, M. Gallinaro, J. Galyardt, F. Garberson, J. E. Garcia, A. F. Garfinkel, P. Garosi, K. Genser, H. Gerberich, D. Gerdes, A. Gessler, S. Giagu, V. Giakoumopoulou, P. Giannetti, K. Gibson, J. L. Gimmell, C. M. Ginsburg, N. Giokaris, M. Giordani, P. Giromini, M. Giunta, G. Giurgiu, V. Glagolev, D. Glenzinski, M. Gold, N. Goldschmidt, A. Golossanov, G. Gomez, G. Gomez-Ceballos, M. Goncharov, O. Gonzalez, I. Gorelov, A. T. Goshaw, K. Goulianos, A. Gresele, S. Grinstein, C. Grosso-Pilcher, R. C. Group, U. Grundler, J. G. da Costa, Z. Gunay-Unalan, C. Haber, K. Hahn, S.

R. Hahn, E. Halkiadakis, B. Y. Han, J. Y. Han, F. Happacher, K. Hara, D. Hare, M. Hare, R. F. Harr, M. Hartz, K. Hatakeyama, C. Hays, M. Heck, J. Heinrich, C. Henderson, M. Herndon, J. Heuser, S. Hewamanage, D. Hidas, C. S. Hill, D. Hirschbuehl, A. Hocker, S. Hou, M. Houlden, S. C. Hsu, B. T. Huffman, R. E. Hughes, M. Hurwitz, U. Husemann, M. Hussein, J. Huston, J. Incandela, G. Introzzi, M. Iori, A. Ivanov, E. James, D. Jang, B. Jayatilaka, E. J. Jeon, M. K. Jha, S. Jindariani, W. Johnson, M. Jones, K. K. Joo, S. Y. Jun, J. E. Jung, T. R. Junk, T. Kamon, D. Kar, P. E. Karchin, Y. Kato, R. Kephart, W. Ketchum, J. Keung, V. Khotilovich, B. Kilminster, D. H. Kim, H. S. Kim, H. W. Kim, J. E. Kim, M. J. Kim, S. B. Kim, S. H. Kim, Y. K. Kim, N. Kimura, L. Kirsch, S. Klimenko, B. Knuteson, K. Kondo, D. J. Kong, J. Konigsberg, A. Korytov, A. V. Kotwal, M. Kreps, J. Kroll, D. Krop, N. Krumnack, M. Kruse, V. Krutelyov, T. Kuhr, N. P. Kulkarni, M. Kurata, S. Kwang, A. T. Laasanen, S. Lami, S. Lammel, M. Lancaster, R. L. Lander, K. Lannon, A. Lath, G. Latino, I. Lazzizzera, T. LeCompte, E. Lee, H. S. Lee, J. S. Lee, S. W. Lee, S. Leone, J. D. Lewis, C. J. Lin, J. Linacre, M. Lindgren, E. Lipeles, A. Lister, D. O. Litvintsev, C. Liu, T. Liu, N. S. Lockyer, A. Loginov, L. Lovas, D. Lucchesi, J. Lueck, P. Lujan, P. Lukens, G. Lungu, J. Lys, R. Lysak, D. MacQueen, R. Madrak, K. Maeshima, K. Makhoul, P. Maksimovic, S. Malde, S. Malik, G. Manca, A. Manousakis-Katsikakis, F. Margaroli, C. Marino, C. P. Marino, A. Martin, V. Martin, M. Martinez, R. Martinez-Ballarin, P. Mastrandrea, M. Mathis, M. E. Mattson, P. Mazzanti, K. S. McFarland, P. McIntyre, R. McNulty, A. Mehta, P. Mehtala, A. Menzione, C. Mesropian, T. Miao, D. Mietlicki, N. Miladinovic, R. Miller, C. Mills, M. Milnik, A. Mitra, G. Mitselmakher, H. Miyake, S. Moed, N. Moggi, M. N. Mondragon, C. S. Moon, R. Moore, M. J. Morello, J. Morlock, P. M. Fernandez, J. Mulmenstadt, A. Mukherjee, T. Muller, P. Murat, M. Mussini, J. Nachtman, Y. Nagai, J. Naganoma, K. Nakamura, I. Nakano, A. Napier, J. Nett, C. Neu, M. S. Neubauer, S. Neubauer, J. Nielsen, L. Nodulman, M. Norman, O. Norniella, E. Nurse, L. Oakes, S. H. Oh, Y. D. Oh, I. Oksuzian, T. Okusawa, R. Orava, K. Osterberg, S. P. Griso, C. Pagliarone, E. Palencia, V. Papadimitriou, A. Papaikonomou, A. A. Paramanov, B. Parks, S. Pashapour, J. Patrick, G. Pauletta, M. Paulini, C. Paus, T. Peiffer, D. E. Pellett, A. Penzo, T. J. Phillips, G. Piacentino, E. Pianori, L. Pinera, K. Pitts, C. Plager, L. Pondrom, K. Potamianos, O. Poukhov, F. Prokoshin, A. Pronko, F. Ptohos, E. Pueschel, G. Punzi, J. Pursley, J. Rademacker, A. Rahaman, V. Ramakrishnan, N. Ranjan, I. Redondo, P. Renton, M. Renz, M. Rescigno, S. Richter, F. Rimondi, L. Ristori, A. Robson, T. Rodrigo, T. Rodriguez, E. Rogers, S. Rolli, R. Roser, M. Rossi, R. Rossin, P. Roy, A. Ruiz, J. Russ, V. Rusu, B. Rutherford, H. Saarikko, A. Safonov, W. K. Sakumoto, L. Santi, L. Sartori, K. Sato, A. Savoy-Navarro, P. Schlabach, A. Schmidt, E. E. Schmidt, M. A. Schmidt, M. P. Schmidt, M. Schmitt, T. Schwarz, L. Scodellaro, A. Scribano, F. Scuri, A. Sedov, S. Seidel, Y. Seiya, A. Semenov, L. Sexton-Kennedy, F. Sforza, A. Sfyrla, S. Z. Shalhout, T. Shears, P. F. Shepard, M. Shimojima, S. Shiraishi, M. Shochet, Y. Shon, I. Shreyber, A. Simonenko, P. Sinervo, A. Sisakyan, A. J. Slaughter, J. Slaunwhite, K. Sliwa, J. R. Smith, F. D. Snider, R. Snihur, A. Soha, S. Somalwar, V. Sorin, T. Spreitzer, P. Squillacioti, M.

Stanitzki, R. St Denis, B. Stelzer, O. Stelzer-Chilton, D. Stentz, J. Strologas, G. L. Strycker, J. S. Suh, A. Sukhanov, I. Suslov, A. Taffard, R. Takashima, Y. Takeuchi, R. Tanaka, J. Tang, M. Tecchio, P. K. Teng, J. Thom, J. Thome, G. A. Thompson, E. Thomson, P. Tipton, P. Ttito-Guzman, S. Tkaczyk, D. Toback, S. Tokar, K. Tollefson, T. Tomura, D. Tonelli, S. Torre, D. Torretta, P. Totaro, S. Tourneur, M. Trovato, S. Y. Tsai, Y. Tu, N. Turini, F. Ukegawa, S. Uozumi, N. van Remortel, A. Varganov, E. Vataga, F. Vazquez, G. Velev, C. Vellidis, M. Vidal, I. Vila, R. Vilar, M. Vogel, I. Volobouev, G. Volpi, P. Wagner, R. G. Wagner, R. L. Wagner, W. Wagner, J. Wagner-Kuhr, T. Wakisaka, R. Wallny, S. M. Wang, A. Warburton, D. Waters, M. Weinberger, J. Weinelt, W. C. Wester, B. Whitehouse, D. Whiteson, A. B. Wicklund, E. Wicklund, S. Wilbur, G. Williams, H. H. Williams, P. Wilson, B. L. Winer, P. Wittich, S. Wolbers, C. Wolfe, H. Wolfe, T. Wright, X. Wu, F. Wurthwein, S. Xie, A. Yagil, K. Yamamoto, J. Yamaoka, U. K. Yang, Y. C. Yang, W. M. Yao, G. P. Yeh, K. Yi, J. Yoh, K. Yorita, T. Yoshida, G. B. Yu, I. Yu, S. S. Yu, J. C. Yun, A. Zanetti, Y. Zeng, X. Zhang, Y. Zheng, and S. Zucchelli

Measurement of the top quark mass and $p\bar{p} \to t\bar{t}$ cross section in the all-hadronic mode with the CDF II detector

T. Aaltonen,[24] J. Adelman,[14] B. Álvarez González,[12,x] S. Amerio,[44b,44a] D. Amidei,[35] A. Anastassov,[39] A. Annovi,[20] J. Antos,[15] G. Apollinari,[18] J. Appel,[18] A. Apresyan,[49] T. Arisawa,[58] A. Artikov,[16] J. Asaadi,[54] W. Ashmanskas,[18] A. Attal,[4] A. Aurisano,[54] F. Azfar,[43] W. Badgett,[18] A. Barbaro-Galtieri,[a29] V. E. Barnes,[49] B. A. Barnett,[26] P. Barria,[47c,47a] P. Bartos,[15] G. Bauer,[33] P.-H. Beauchemin,[34] F. Bedeschi,[47a] D. Beecher,[31] S. Behari,[26] G. Bellettini,[47b,47a] J. Bellinger,[60] D. Benjamin,[17] A. Beretvas,[18] A. Bhatti,[51] M. Binkley,[18] D. Bisello,[44b,44a] I. Bizjak,[31,ee] R. E. Blair,[2] C. Blocker,[7] B. Blumenfeld,[26] A. Bocci,[17] A. Bodek,[50] V. Boisvert,[50] D. Bortoletto,[49] J. Boudreau,[48] A. Boveia,[11] B. Brau,[11,b] A. Bridgeman,[25] L. Brigliadori,[6b,6a] C. Bromberg,[36] E. Brubaker,[14] J. Budagov,[16] H. S. Budd,[50] S. Budd,[25] K. Burkett,[18] G. Busetto,[44b,44a] P. Bussey,[22] A. Buzatu,[34] K. L. Byrum,[2] S. Cabrera,[17,z] C. Calancha,[32] S. Camarda,[4] M. Campanelli,[31] M. Campbell,[35] F. Canelli,[14,18] A. Canepa,[46] B. Carls,[25] D. Carlsmith,[60] R. Carosi,[47a] S. Carrillo,[19,o] S. Carron,[18] B. Casal,[12] M. Casarsa,[18] A. Castro,[6b,6a] P. Catastini,[47c,47a] D. Cauz,[55a] V. Cavaliere,[47c,47a] M. Cavalli-Sforza,[4] A. Cerri,[a29] L. Cerrito,[31,r] S. H. Chang,[28] Y. C. Chen,[1] M. Chertok,[8] G. Chiarelli,[47a] G. Chlachidze,[18] F. Chlebana,[18] K. Cho,[28] D. Chokheli,[16] J. P. Chou,[23] K. Chung,[18,p] W. H. Chung,[60] Y. S. Chung,[50] T. Chwalek,[27] C. I. Ciobanu,[45] M. A. Ciocci,[47c,47a] A. Clark,[21] D. Clark,[7] G. Compostella,[44a] M. E. Convery,[18] J. Conway,[8] M. Corbo,[45] M. Cordelli,[20] C. A. Cox,[8] D. J. Cox,[8] F. Crescioli,[47b,47a] C. Cuenca Almenar,[61] J. Cuevas,[12,x] R. Culbertson,[18] J. C. Cully,[35] D. Dagenhart,[18] N. d'Ascenzo,[45,w] M. Datta,[18] T. Davies,[22] P. de Barbaro,[50] S. De Cecco,[52a] A. Deisher,[a29] G. De Lorenzo,[4] M. Dell'Orso,[47b,47a] C. Deluca,[4] L. Demortier,[51] J. Deng,[17,g] M. Deninno,[6a] M. d'Errico,[44b,44a] A. Di Canto,[47b,47a] B. Di Ruzza,[47a] J. R. Dittmann,[5] M. D'Onofrio,[4] S. Donati,[47b,47a] P. Dong,[18] T. Dorigo,[44a] S. Dube,[53] K. Ebina,[58] A. Elagin,[54] R. Erbacher,[8] D. Errede,[25] S. Errede,[25] N. Ershaidat,[45,dd] R. Eusebi,[54] H. C. Fang,[a29] S. Farrington,[43] W. T. Fedorko,[14] R. G. Feild,[61] M. Feindt,[27] J. P. Fernandez,[32] C. Ferrazza,[47d,47a] R. Field,[19] G. Flanagan,[49,t] R. Forrest,[8] M. J. Frank,[5] M. Franklin,[23] J. C. Freeman,[18] I. Furic,[19] M. Gallinaro,[51] J. Galyardt,[13] F. Garberson,[11] J. E. Garcia,[21] A. F. Garfinkel,[49] P. Garosi,[47c,47a] H. Gerberich,[25] D. Gerdes,[35] A. Gessler,[27] S. Giagu,[52b,52a] V. Giakoumopoulou,[3] P. Giannetti,[47a] K. Gibson,[48] J. L. Gimmell,[50] C. M. Ginsburg,[18] N. Giokaris,[3] M. Giordani,[55b,55a] P. Giromini,[20] M. Giunta,[47a] G. Giurgiu,[26] V. Glagolev,[16] D. Glenzinski,[18] M. Gold,[38] N. Goldschmidt,[19] A. Golossanov,[18] G. Gomez,[12] G. Gomez-Ceballos,[33] M. Goncharov,[33] O. González,[32] I. Gorelov,[38] A. T. Goshaw,[17] K. Goulianos,[51] A. Gresele,[44b,44a] S. Grinstein,[4] C. Grosso-Pilcher,[14] R. C. Group,[18] U. Grundler,[25] J. Guimaraes da Costa,[23] Z. Gunay-Unalan,[36] C. Haber,[a29] S. R. Hahn,[18] E. Halkiadakis,[53] B.-Y. Han,[50] J. Y. Han,[50] F. Happacher,[20] K. Hara,[56] D. Hare,[53] M. Hare,[57] R. F. Harr,[59] M. Hartz,[48] K. Hatakeyama,[5] C. Hays,[43] M. Heck,[27] J. Heinrich,[46] M. Herndon,[60] J. Heuser,[27] S. Hewamanage,[5] D. Hidas,[53] C. S. Hill,[11,d] D. Hirschbuehl,[27] A. Hocker,[18] S. Hou,[1] M. Houlden,[30] S.-C. Hsu,[a29] R. E. Hughes,[40] M. Hurwitz,[14] U. Husemann,[61] M. Hussein,[36] J. Huston,[36] J. Incandela,[11] G. Introzzi,[47a] M. Iori,[52b,52a] A. Ivanov,[8,q] E. James,[18] D. Jang,[13] B. Jayatilaka,[17] E. J. Jeon,[28] M. K. Jha,[6a] S. Jindariani,[18] W. Johnson,[8] M. Jones,[49] K. K. Joo,[28] S. Y. Jun,[13] J. E. Jung,[28] T. R. Junk,[18] T. Kamon,[54] D. Kar,[19] P. E. Karchin,[59] Y. Kato,[42,n] R. Kephart,[18] W. Ketchum,[14] J. Keung,[46] V. Khotilovich,[54] B. Kilminster,[18] D. H. Kim,[28] H. S. Kim,[28] H. W. Kim,[28] J. E. Kim,[28] M. J. Kim,[20] S. B. Kim,[28] S. H. Kim,[56] Y. K. Kim,[14] N. Kimura,[58] L. Kirsch,[7] S. Klimenko,[19] K. Kondo,[58] D. J. Kong,[28] J. Konigsberg,[19] A. Korytov,[19] A. V. Kotwal,[17] M. Kreps,[27] J. Kroll,[46] D. Krop,[14] N. Krumnack,[5] M. Kruse,[17] V. Krutelyov,[11] T. Kuhr,[27] N. P. Kulkarni,[59] M. Kurata,[56] S. Kwang,[14] A. T. Laasanen,[49] S. Lami,[47a] S. Lammel,[18] M. Lancaster,[31] R. L. Lander,[8] K. Lannon,[40,v] A. Lath,[53] G. Latino,[47c,47a] I. Lazzizzera,[44b,44a] T. LeCompte,[2] E. Lee,[54] H. S. Lee,[14] J. S. Lee,[28] S. W. Lee,[54,y] S. Leone,[47a] J. D. Lewis,[18] C.-J. Lin,[a29] J. Linacre,[43] M. Lindgren,[18] E. Lipeles,[46] A. Lister,[21] D. O. Litvintsev,[18] C. Liu,[48] T. Liu,[18] N. S. Lockyer,[46] A. Loginov,[61] L. Lovas,[15] D. Lucchesi,[44b,44a] J. Lueck,[27] P. Lujan,[a29] P. Lukens,[18] G. Lungu,[51] J. Lys,[a29] R. Lysak,[15] D. MacQueen,[34] R. Madrak,[18] K. Maeshima,[18] K. Makhoul,[33] P. Maksimovic,[26] S. Malde,[43] S. Malik,[31] G. Manca,[30,f] A. Manousakis-Katsikakis,[3] F. Margaroli,[49] C. Marino,[27] C. P. Marino,[25] A. Martin,[61] V. Martin,[22,l] M. Martínez,[4] R. Martínez-Ballarín,[32] P. Mastrandrea,[52a] M. Mathis,[26] M. E. Mattson,[59] P. Mazzanti,[6a] K. S. McFarland,[50] P. McIntyre,[54] R. McNulty,[30,k] A. Mehta,[30] P. Mehtala,[24] A. Menzione,[47a] C. Mesropian,[51] T. Miao,[18] D. Mietlicki,[35] N. Miladinovic,[7] R. Miller,[36] C. Mills,[23] M. Milnik,[27] A. Mitra,[1] G. Mitselmakher,[19] H. Miyake,[56] S. Moed,[23] N. Moggi,[6a] M. N. Mondragon,[18,o] C. S. Moon,[28] R. Moore,[18] M. J. Morello,[47a] J. Morlock,[27] P. Movilla Fernandez,[18] J. Mülmenstädt,[a29] A. Mukherjee,[18] Th. Muller,[27] P. Murat,[18] M. Mussini,[6b,6a] J. Nachtman,[18,p] Y. Nagai,[56] J. Naganoma,[56] K. Nakamura,[56] I. Nakano,[41] A. Napier,[57] J. Nett,[60] C. Neu,[46,bb] M. S. Neubauer,[25] S. Neubauer,[27] J. Nielsen,[a29,h] L. Nodulman,[2] M. Norman,[10] O. Norniella,[25] E. Nurse,[31] L. Oakes,[43] S. H. Oh,[17] Y. D. Oh,[28] I. Oksuzian,[19] T. Okusawa,[42] R. Orava,[24] K. Osterberg,[24] S. Pagan Griso,[44b,44a]

C. Pagliarone,[55a] E. Palencia,[18] V. Papadimitriou,[18] A. Papaikonomou,[27] A. A. Paramanov,[2] B. Parks,[40] S. Pashapour,[34] J. Patrick,[18] G. Pauletta,[55b,55a] M. Paulini,[13] C. Paus,[33] T. Peiffer,[27] D. E. Pellett,[8] A. Penzo,[55a] T. J. Phillips,[17] G. Piacentino,[47a] E. Pianori,[46] L. Pinera,[19] K. Pitts,[25] C. Plager,[9] L. Pondrom,[60] K. Potamianos,[49] O. Poukhov,[16,a] F. Prokoshin,[16,aa] A. Pronko,[18] F. Ptohos,[18,j] E. Pueschel,[13] G. Punzi,[47b,47a] J. Pursley,[60] J. Rademacker,[43,d] A. Rahaman,[48] V. Ramakrishnan,[60] N. Ranjan,[49] I. Redondo,[32] P. Renton,[43] M. Renz,[27] M. Rescigno,[52a] S. Richter,[27] F. Rimondi,[6b,6a] L. Ristori,[47a] A. Robson,[22] T. Rodrigo,[12] T. Rodriguez,[46] E. Rogers,[25] S. Rolli,[57] R. Roser,[18] M. Rossi,[55a] R. Rossin,[11] P. Roy,[34] A. Ruiz,[12] J. Russ,[13] V. Rusu,[18] B. Rutherford,[18] H. Saarikko,[24] A. Safonov,[54] W. K. Sakumoto,[50] L. Santi,[55b,55a] L. Sartori,[47a] K. Sato,[56] V. Saveliev,[45,w] A. Savoy-Navarro,[45] P. Schlabach,[18] A. Schmidt,[27] E. E. Schmidt,[18] M. A. Schmidt,[14] M. P. Schmidt,[61,a] M. Schmitt,[39] T. Schwarz,[8] L. Scodellaro,[12] A. Scribano,[47c,47a] F. Scuri,[47a] A. Sedov,[49] S. Seidel,[38] Y. Seiya,[42] A. Semenov,[16] L. Sexton-Kennedy,[18] F. Sforza,[47b,47a] A. Sfyrla,[25] S. Z. Shalhout,[59] T. Shears,[30] P. F. Shepard,[48] M. Shimojima,[56,u] S. Shiraishi,[14] M. Shochet,[14] Y. Shon,[60] I. Shreyber,[37] A. Simonenko,[16] P. Sinervo,[34] A. Sisakyan,[16] A. J. Slaughter,[18] J. Slaunwhite,[40] K. Sliwa,[57] J. R. Smith,[8] F. D. Snider,[18] R. Snihur,[34] A. Soha,[18] S. Somalwar,[53] V. Sorin,[4] P. Squillacioti,[47c,47a] M. Stanitzki,[61] R. St. Denis,[22] B. Stelzer,[34] O. Stelzer-Chilton,[34] D. Stentz,[39] J. Strologas,[38] G. L. Strycker,[35] J. S. Suh,[28] A. Sukhanov,[19] I. Suslov,[16] A. Taffard,[25,g] R. Takashima,[41] Y. Takeuchi,[56] R. Tanaka,[41] J. Tang,[14] M. Tecchio,[35] P. K. Teng,[1] J. Thom,[18,i] J. Thome,[13] G. A. Thompson,[25] E. Thomson,[46] P. Tipton,[61] P. Ttito-Guzmán,[32] S. Tkaczyk,[18] D. Toback,[54] S. Tokar,[15] K. Tollefson,[36] T. Tomura,[56] D. Tonelli,[18] S. Torre,[20] D. Torretta,[18] P. Totaro,[55b,55a] M. Trovato,[47d,47a] S.-Y. Tsai,[1] Y. Tu,[46] N. Turini,[47c,47a] F. Ukegawa,[56] S. Uozumi,[28] N. van Remortel,[24,c] A. Varganov,[35] E. Vataga,[47d,47a] F. Vázquez,[19,o] G. Velev,[18] C. Vellidis,[3] M. Vidal,[32] I. Vila,[12] R. Vilar,[12] M. Vogel,[38] I. Volobouev,[a29,y] G. Volpi,[47a,47a] P. Wagner,[46] R. G. Wagner,[2] R. L. Wagner,[18] W. Wagner,[27,cc] J. Wagner-Kuhr,[27] T. Wakisaka,[42] R. Wallny,[9] S. M. Wang,[1] A. Warburton,[34] D. Waters,[31] M. Weinberger,[54] J. Weinelt,[27] W. C. Wester III,[18] B. Whitehouse,[57] D. Whiteson,[46,g] A. B. Wicklund,[2] E. Wicklund,[18] S. Wilbur,[14] G. Williams,[34] H. H. Williams,[46] P. Wilson,[18] B. L. Winer,[40] P. Wittich,[18,i] S. Wolbers,[18] C. Wolfe,[14] H. Wolfe,[40] T. Wright,[35] X. Wu,[21] F. Würthwein,[10] A. Yagil,[10] K. Yamamoto,[42] J. Yamaoka,[17] U. K. Yang,[14,s] Y. C. Yang,[28] W. M. Yao,[a29] G. P. Yeh,[18] K. Yi,[18,p] J. Yoh,[18] K. Yorita,[58] T. Yoshida,[42,m] G. B. Yu,[17] I. Yu,[28] S. S. Yu,[18] J. C. Yun,[18] A. Zanetti,[55a] Y. Zeng,[17] X. Zhang,[25] Y. Zheng,[9,e] and S. Zucchelli[6b,6a]

(CDF Collaboration)

[1]*Institute of Physics, Academia Sinica, Taipei, Taiwan 11529, Republic of China*
[2]*Argonne National Laboratory, Argonne, Illinois 60439, USA*
[3]*University of Athens, 157 71 Athens, Greece*
[4]*Institut de Fisica d'Altes Energies, Universitat Autonoma de Barcelona, E-08193, Bellaterra (Barcelona), Spain*
[5]*Baylor University, Waco, Texas 76798, USA*
[6a]*Istituto Nazionale di Fisica Nucleare Bologna, I-40127 Bologna, Italy*
[6b]*University of Bologna, I-40127 Bologna, Italy*
[7]*Brandeis University, Waltham, Massachusetts 02254, USA*
[8]*University of California, Davis, Davis, California 95616, USA*
[9]*University of California, Los Angeles, Los Angeles, California 90024, USA*
[10]*University of California, San Diego, La Jolla, California 92093, USA*
[11]*University of California, Santa Barbara, Santa Barbara, California 93106, USA*
[12]*Instituto de Fisica de Cantabria, CSIC-University of Cantabria, 39005 Santander, Spain*
[13]*Carnegie Mellon University, Pittsburgh, Pennsylvania 15213, USA*
[14]*Enrico Fermi Institute, University of Chicago, Chicago, Illinois 60637, USA*
[15]*Comenius University, 842 48 Bratislava, Slovakia;*
Institute of Experimental Physics, 040 01 Kosice, Slovakia
[16]*Joint Institute for Nuclear Research, RU-141980 Dubna, Russia*
[17]*Duke University, Durham, North Carolina 27708, USA*
[18]*Fermi National Accelerator Laboratory, Batavia, Illinois 60510*
[19]*University of Florida, Gainesville, Florida 32611, USA*
[20]*Laboratori Nazionali di Frascati, Istituto Nazionale di Fisica Nucleare, I-00044 Frascati, Italy*
[21]*University of Geneva, CH-1211 Geneva 4, Switzerland*
[22]*Glasgow University, Glasgow G12 8QQ, United Kingdom*
[23]*Harvard University, Cambridge, Massachusetts 02138, USA*
[24]*Division of High Energy Physics, Department of Physics, University of Helsinki and Helsinki Institute of Physics, FIN-00014, Helsinki, Finland*

[25]University of Illinois, Urbana, Illinois 61801, USA
[26]The Johns Hopkins University, Baltimore, Maryland 21218, USA
[27]Institut für Experimentelle Kernphysik, Karlsruhe Institute of Technology, D-76131 Karlsruhe, Germany
[28]Center for High Energy Physics: Kyungpook National University, Daegu 702-701, Korea;
Seoul National University, Seoul 151-742, Korea;
Sungkyunkwan University, Suwon 440-746, Korea;
Korea Institute of Science and Technology Information, Daejeon 305-806, Korea;
Chonnam National University, Gwangju 500-757, Korea;
Chonbuk National University, Jeonju 561-756, Korea
[a29]Ernest Orlando Lawrence Berkeley National Laboratory, Berkeley, California 94720, USA
[30]University of Liverpool, Liverpool L69 7ZE, United Kingdom
[31]University College London, London WC1E 6BT, United Kingdom
[32]Centro de Investigaciones Energeticas Medioambientales y Tecnologicas, E-28040 Madrid, Spain
[33]Massachusetts Institute of Technology, Cambridge, Massachusetts 02139, USA
[34]Institute of Particle Physics: McGill University, Montréal, Québec, Canada H3A 2T8;
Simon Fraser University, Burnaby, British Columbia, Canada V5A 1S6;
University of Toronto, Toronto, Ontario, Canada M5S 1A7;
and TRIUMF, Vancouver, British Columbia, Canada V6T 2A3
[35]University of Michigan, Ann Arbor, Michigan 48109, USA
[36]Michigan State University, East Lansing, Michigan 48824, USA
[37]Institution for Theoretical and Experimental Physics, ITEP, Moscow 117259, Russia
[38]University of New Mexico, Albuquerque, New Mexico 87131, USA
[39]Northwestern University, Evanston, Illinois 60208, USA
[40]The Ohio State University, Columbus, Ohio 43210, USA
[41]Okayama University, Okayama 700-8530, Japan
[42]Osaka City University, Osaka 588, Japan
[43]University of Oxford, Oxford OX1 3RH, United Kingdom
[44a]Istituto Nazionale di Fisica Nucleare, Sezione di Padova-Trento, I-35131 Padova, Italy
[44b]University of Padova, I-35131 Padova, Italy
[45]LPNHE, Universite Pierre et Marie Curie/IN2P3-CNRS, UMR7585, Paris, F-75252 France
[46]University of Pennsylvania, Philadelphia, Pennsylvania 19104, USA
[47a]Istituto Nazionale di Fisica Nucleare Pisa, I-56127 Pisa, Italy

[a]Deceased.

[b]Visitor from University of Massachusetts Amherst, Amherst, MA 01003, USA.

[c]Visitor from Universiteit Antwerpen, B-2610 Antwerp, Belgium.

[d]Visitor from University of Bristol, Bristol BS8 1TL, United Kingdom.

[e]Visitor from Chinese Academy of Sciences, Beijing 100864, China.

[f]Visitor from Istituto Nazionale di Fisica Nucleare, Sezione di Cagliari, 09042 Monserrato (Cagliari), Italy.

[g]Visitor from University of California Irvine, Irvine, CA 92697, USA.

[h]Visitor from University of California Santa Cruz, Santa Cruz, CA 95064, USA

[i]Visitor from Cornell University, Ithaca, NY 14853, USA.

[j]Visitor from University of Cyprus, Nicosia CY-1678, Cyprus.

[k]Visitor from University College Dublin, Dublin 4, Ireland.

[l]Visitor from University of Edinburgh, Edinburgh EH9 3JZ, United Kingdom.

[m]Visitor from University of Fukui, Fukui City, Fukui Prefecture, Japan 910-0017.

[n]Visitor from Kinki University, Higashi-Osaka City, Japan 577-8502.

[o]Visitor from Universidad Iberoamericana, Mexico D.F., Mexico.

[p]Visitor from University of Iowa, Iowa City, IA 52242, USA.

[q]Visitor from Kansas State University, Manhattan, KS 66506, USA.

[r]Visitor from Queen Mary, University of London, London, E1 4NS, England.

[s]Visitor from University of Manchester, Manchester M13 9PL, England.

[t]Visitor from Muons, Inc., Batavia, IL 60510, USA.

[u]Visitor from Nagasaki Institute of Applied Science, Nagasaki, Japan.

[v]Visitor from University of Notre Dame, Notre Dame, IN 46556, USA.

[w]Visitor from Obninsk State University, Obninsk, Russia.

[x]Visitor from University de Oviedo, E-33007 Oviedo, Spain.

[y]Visitor from Texas Tech University, Lubbock, TX 79609, USA.

[z]Visitor from IFIC (CSIC-Universitat de Valencia), 56071 Valencia, Spain.

[aa]Visitor from Universidad Tecnica Federico Santa Maria, 110v Valparaiso, Chile.

[bb]Visitor from University of Virginia, Charlottesville, VA 22906, USA.

[cc]Visitor from Bergische Universität Wuppertal, 42097 Wuppertal, Germany.

[dd]Visitor from Yarmouk University, Irbid 211-63, Jordan.

[ee]On leave from J. Stefan Institute, Ljubljana, Slovenia.

[47b]*University of Pisa, I-56127 Pisa, Italy*
[47c]*University of Siena, I-56127 Pisa, Italy*
[47d]*Scuola Normale Superiore, I-56127 Pisa, Italy*
[48]*University of Pittsburgh, Pittsburgh, Pennsylvania 15260, USA*
[49]*Purdue University, West Lafayette, Indiana 47907, USA*
[50]*University of Rochester, Rochester, New York 14627, USA*
[51]*The Rockefeller University, New York, New York 10021, USA*
[52a]*Istituto Nazionale di Fisica Nucleare, Sezione di Roma 1, I-00185 Roma, Italy*
[52b]*Sapienza Università di Roma, I-00185 Roma, Italy*
[53]*Rutgers University, Piscataway, New Jersey 08855, USA*
[54]*Texas A&M University, College Station, Texas 77843, USA*
[55a]*Istituto Nazionale di Fisica Nucleare Trieste/Udine, I-34100 Trieste, I-33100 Udine, Italy*
[55b]*University of Trieste/Udine, I-33100 Udine, Italy*
[56]*University of Tsukuba, Tsukuba, Ibaraki 305, Japan*
[57]*Tufts University, Medford, Massachusetts 02155, USA*
[58]*Waseda University, Tokyo 169, Japan*
[59]*Wayne State University, Detroit, Michigan 48201, USA*
[60]*University of Wisconsin, Madison, Wisconsin 53706, USA*
[61]*Yale University, New Haven, Connecticut 06520, USA*
(Received 3 February 2010; published 30 March 2010)

We present a measurement of the top quark mass and of the top-antitop ($t\bar{t}$) pair production cross section using $p\bar{p}$ data collected with the CDF II detector at the Tevatron Collider at the Fermi National Accelerator Laboratory and corresponding to an integrated luminosity of 2.9 fb^{-1}. We select events with six or more jets satisfying a number of kinematical requirements imposed by means of a neural-network algorithm. At least one of these jets must originate from a b quark, as identified by the reconstruction of a secondary vertex inside the jet. The mass measurement is based on a likelihood fit incorporating reconstructed mass distributions representative of signal and background, where the absolute jet energy scale (JES) is measured simultaneously with the top quark mass. The measurement yields a value of $174.8 \pm 2.4(\text{stat} + \text{JES})^{+1.2}_{-1.0}(\text{syst})$ GeV$/c^2$, where the uncertainty from the absolute jet energy scale is evaluated together with the statistical uncertainty. The procedure also measures the amount of signal from which we derive a cross section, $\sigma_{t\bar{t}} = 7.2 \pm 0.5(\text{stat}) \pm 1.0(\text{syst}) \pm 0.4(\text{lum})$ pb, for the measured values of top quark mass and JES.

DOI: 10.1103/PhysRevD.81.052011 PACS numbers: 14.65.Ha, 13.85.Ni, 13.85.Qk

I. INTRODUCTION

Since its early measurements, the large value of the top quark mass (M_{top}) has represented a really striking property of this particle, giving to the top quark a special position within the standard model (SM) and suggesting also possible links to new physics [1]. In fact, apart from being itself a fundamental parameter of the SM, M_{top} is by far the largest mass among the ones of the observed fermions, and this makes the top quark contribution dominant in higher order corrections to many observables. Therefore M_{top} plays a central role in checking the consistency of theoretical predictions of the SM. The higher order corrections apply also to the W boson propagator, and therefore affect the calculated value of the W mass, M_W. As the latter depends logarithmically on the mass of the Higgs boson, precise measurements of M_W and M_{top} allow setting indirect constraints on the value of the mass of this fundamental, but still unobserved particle [2]. Moreover, possible contributions due to some unknown physics might also be constrained. Finally, the present value of M_{top} makes the Yukawa coupling to the Higgs field of $\mathcal{O}(1)$ and this could indicate a special role of the top quark in the mechanism of electroweak symmetry breaking.

All these reasons make the accurate knowledge of M_{top} a really important issue, but the same is true for the measurement of the $t\bar{t}$ production cross section ($\sigma_{t\bar{t}}$), both as a test for physics contributions beyond the SM and as a test of current next-to-leading-order (NLO) QCD calculations [3]. Usually, measurements of $\sigma_{t\bar{t}}$ rely upon event counting and are performed assuming an *a priori* value for M_{top}. The technique used here allows the simultaneous measurement of both these important and related properties of the top quark.

At the Tevatron Collider at Fermi National Accelerator Laboratory, top quarks are produced mostly in pairs. In the SM the top quark decays into a W boson and a b quark almost 100% of the time, and the topology of the final state resulting from a $t\bar{t}$ event depends on the hadronic or leptonic decay of the two final-state W bosons. In this paper, we consider events characterized by a multijet topology (*all-hadronic* mode) with no energetic leptons. This

$t\bar{t}$ final state has the advantage of a large branching ratio ($\approx 4/9$) and of having no undetectable final-state particles. The major challenge of this channel is the large background from QCD multijet production, which dominates the signal by 3 orders of magnitude after the application of a specific online event selection (trigger). To increase the purity of the candidate sample, requirements based on the kinematical and topological characteristics of SM $t\bar{t}$ events are expressed in terms of an artificial neural network and applied to the data. Further improvement is then obtained from the requirement of at least one jet identified as originating from a b quark using a secondary vertex b-tagging algorithm. Simulations predict that a clear $t\bar{t}$ signal will thus become visible over background in the selected data sample, and the measurement of the top quark mass and the $t\bar{t}$ cross section is made possible in spite of the overwhelming QCD multijet production.

A reconstructed top quark mass is determined by fitting the kinematics of the six leading jets in the event to a $t\bar{t}$ final state. This variable, denoted as m_t^{rec}, does not strictly represent a measurement of M_{top}, but its distribution obtained by a sample of $t\bar{t}$ events is sensitive to M_{top} itself. The jet energy scale (JES) is a factor representing the set of corrections needed to obtain a better estimate of the energy of a parton starting from a jet reconstructed by clusters in the calorimeter. The default JES used in simulated events is obtained by a tuning to the data, but possible discrepancies between data and simulation lead to an uncertainty on this value. The strong correlation existing between the m_t^{rec} distribution and the JES implies therefore a corresponding uncertainty on M_{top}. However, the JES can be calibrated using the selected samples of $t\bar{t}$ candidate events, where a second variable, m_W^{rec}, is reconstructed by the four-momenta of the jets assigned to the W bosons. This variable is related to the well-known value of the W-boson mass, and the JES can be adjusted in such a way that both the m_t^{rec} and the m_W^{rec} distributions for simulated events match the observed data. The inclusion of this procedure, usually referred to as *in situ* calibration, enables a significant reduction of the systematic uncertainty associated with the inaccurate knowledge of the JES, and represents an important improvement of the work described in this paper with respect to the previous CDF analysis by a similar method [4].

The m_t^{rec} and m_W^{rec} distributions are reconstructed in two separate samples of selected data events, defined by the presence of exactly one and two or more b-tagged jets, respectively. The data are then compared to corresponding distributions expected from background and $t\bar{t}$ events simulated with various values of the top quark mass and of the JES to fit for these parameters. In addition, the fitted signal yields are used to derive a measurement of the $t\bar{t}$ production cross section.

The results reported here are based on data taken between March 2002 and April 2008, corresponding to an integrated luminosity of 2.9 fb^{-1}. This measurement complements other recent determinations of the top quark mass and $t\bar{t}$ cross section by CDF and D0 [5,6] in other final states, and improves the latest CDF measurements in the same channel [4,7].

The organization of the paper is as follows: Section II contains a brief description of the CDF II detector. The trigger and the neural-network-based sample selection are discussed in Sec. III, along with the identification of jets initiated by b quarks (b jets). Sections IV and V present the simulated signal samples and the data-driven method we use for estimating the background from multijet data. Section VI describes how the fundamental variables m_t^{rec} and m_W^{rec} are reconstructed, while in Sec. VII we present the final requirements to define the samples of events used in the measurement. The parametrization of the dependence of the distributions of reconstructed variables on the values of the top quark mass and the jet energy scale are described in Sec. VIII A. The fit to the experimental distributions and its calibration are described in Secs. VIII B and IX, respectively. Section X details the study of the systematic uncertainties on the mass measurement, which is then reported in Sec. XI. We describe in Sec. XII the measurement of the $t\bar{t}$ cross section.

II. THE CDF II DETECTOR

The CDF II detector [8] is an azimuthally and forward-backward symmetric apparatus designed to study $p\bar{p}$ collisions at the Tevatron. A cylindrical coordinate system is used where θ is the polar angle to the proton beam direction at the event vertex, ϕ is the azimuthal angle about the beam axis, and pseudorapidity is defined as $\eta = -\ln[\tan(\theta/2)]$. We define transverse energy as $E_T = E\sin\theta$ and transverse momentum as $p_T = p\sin\theta$, where E is the energy measured by calorimeters, and p is the magnitude of the momentum measured by a tracking system. The detector consists of a magnetic spectrometer surrounded by calorimeters and muon chambers. The charged particle tracking system is immersed in a 1.4 T solenoidal magnetic field with axis parallel to the beam line. A set of silicon microstrip detectors provides charged particle tracking in the radial range from 1.5 to 28 cm, while a 3.1 m long open-cell drift chamber, the central outer tracker (COT), covers the radial range from 40 to 137 cm. In combination, the silicon and COT detectors provide excellent tracking up to about pseudorapidities $|\eta| \leq 1.1$, and with decreasing precision up to $|\eta| \leq 2.0$. Segmented electromagnetic and hadronic calorimeters surround the tracking system, and measure the energy deposit of particles interacting in the calorimeters. The electromagnetic and hadronic calorimeters are lead-scintillator and iron-scintillator sampling devices, respectively, covering the range $|\eta| \leq 3.6$. They are segmented in the central region ($|\eta| < 1.1$) in towers of 15° in azimuth and 0.1 in η, and the forward region ($1.1 < |\eta| < 3.6$) in towers of 7.5°

for $|\eta| < 2.11$ and 15° for $|\eta| > 2.11$, while the coverage in $|\eta|$ increases gradually from 0.1 to 0.6. The electromagnetic calorimeters [9,10] are instrumented with proportional chambers (at large angles) or scintillating strip detectors (in the forward regions), which measure the transverse profile of electromagnetic showers at a depth corresponding to the expected shower maxima. Drift chambers located outside the central hadronic calorimeters and behind a 60 cm iron shield detect muons with $|\eta| \leq 0.6$ [11]. Additional drift chambers and scintillation counters detect muons in the region $0.6 < |\eta| < 1.5$. Multicell gas Cherenkov counters [12] with a coverage of $3.7 < |\eta| < 4.7$ measure the average number of inelastic $p\bar{p}$ collisions and thereby are used to determine the luminosity.

III. MULTIJET EVENT SELECTION AND *b* TAGGING

The final state of all-hadronic $t\bar{t}$ events is characterized by the presence of at least six jets from the decay of the two top quarks, where additional jets might come from initial- or final-state radiation (ISR or FSR). Events having such a topology are collected using a multijet trigger which relies on calorimeter information. Subsequently, jets are identified during event reconstruction by grouping clusters of energy in the calorimeter using a fixed-cone algorithm with a radius of 0.4 in $\eta - \phi$ space [13]. After a preliminary selection of multijet events, a neural-network selection based on relevant kinematical variables is used to further improve the purity of the sample.

A. Multijet trigger

The CDF trigger system has three levels. The first two levels consist of special-purpose electronic circuits and the third one of conventional programmable digital processors. At level 1, the trigger requires the presence of at least one calorimeter tower with transverse energy $E_T^{\text{tow}} \geq 10$ GeV. At level 2, the total transverse energy, obtained as the sum over all calorimeter towers, $\sum E_T^{\text{tow}}$, must be ≥ 175 GeV. Moreover, the presence of least four clusters of towers, each with transverse energy $E_T^{\text{clus}} \geq 15$ GeV, is required. Finally, the third trigger level confirms the level 2 selection using a more accurate determination of the jet energy, requiring four or more reconstructed jets with $E_T \geq 10$ GeV. Approximately 14×10^6 events satisfy the trigger requirements, corresponding to an events signal-over-background ratio (S/B) of about $1/1200$, assuming a theoretical cross section of 6.7 pb for a top quark mass of 175 GeV$/c^2$ [3].

B. Preselection and topology requirements

Events satisfying the trigger requirements are reconstructed in terms of their final-state observables (tracks, vertices, charged leptons, and jets). We retain only those events that are well contained in detector acceptance, requiring the primary event vertex [14] to lie inside the luminous region ($|z| < 60$ cm). We remove events having well-identified energetic electrons or muons as defined in [15], namely, electrons with $E_T > 20$ GeV and muons with $p_T > 20$ GeV$/c$.

In order to have jets matching as accurately as possible to the hard scattering partons, we correct jet energies for detector response and multiple interactions [16]. First, we consider the η dependence of detector response and energy loss in the uninstrumented regions. Then, after accounting for the small extra energy deposited by multiple collisions in the same beam-beam bunch crossing, a correction for calorimeter nonlinearity is applied so that the jet energies are equal, on average, to the energy of the particles incident on the jet cone. The total uncertainty on the estimate of the original parton energy, where all uncertainties for the individual corrections are added in quadrature, varies from 8% to 3% with jet transverse energy increasing from 15 GeV to 50 GeV, and remains approximately constant at 3% above 50 GeV. Jets with $|\eta| \leq 2$ and $E_T \geq 15$ GeV, after all corrections are applied, are selected for further analysis.

As the uncertainty on the missing transverse energy, $\not\!\!E_T$ [17], increases proportionally to $\sqrt{\sum E_T}$ [18], its significance is defined as $\frac{\not\!\!E_T}{\sqrt{\sum E_T}}$, where the $\not\!\!E_T$ is corrected for any identified muons, while $\sum E_T$ is obtained by summing the E_T's of all the selected jets. We then require that $\frac{\not\!\!E_T}{\sqrt{\sum E_T}}$ be <3 GeV$^{1/2}$ to select events with small $\not\!\!E_T$. At this stage, called preselection, we are left with about 8.2×10^6 events.

As the topology of the candidate events is determined by the jet multiplicity, we define the signal region by selecting events with a number of jets $6 \leq N_{\text{jets}} \leq 8$, and we also require jet pairs to be separated by at least 0.5 units in the $\eta - \phi$ space. The number of events passing these additional requirements is 1.671×10^6, with an expected S/B of approximately $1/430$.

C. Neural-network-based kinematical selection

To further improve the purity of the signal sample, we use a multivariate approach and take advantage of the distinctive features of signal and background events through a neural network, which takes into account the correlations between the kinematical variables which enter as input nodes in the network. The network uses the MLPFIT package [19] as implemented by ROOT [20] through the *TMultiLayer-Perceptron* class.

A first set of 11 global variables, summarized in Table I, have already been proven to be effective [4] in reducing the QCD background. Studies performed for this analysis on the jet development in the calorimeter have indicated that a good discrimination between quark-initiated and gluon-initiated jets can be accomplished with η moments (M_η)

TABLE I. Input variables to the neural network.

Variable	Description
$\sum E_T$	Scalar sum of selected jets E_T
$\sum_3 E_T$	As above, except the two highest-E_T jets
C	Centrality
A	Aplanarity
$M_{2j}^{\min}$	Minimum dijet invariant mass
$M_{2j}^{\max}$	Maximum dijet invariant mass
$M_{3j}^{\min}$	Minimum trijet invariant mass
$M_{3j}^{\max}$	Maximum trijet invariant mass
$E_T^{\star,1}$	$E_T \sin^2\theta^\star$ for the highest-E_T jet
$E_T^{\star,2}$	$E_T \sin^2\theta^\star$ for the next-to-highest-E_T jet
$\langle E_T^\star \rangle$	Geometric mean over the remaining jets
$\langle M_\eta^s \rangle$	Geometric mean over the untagged jets
$\langle M_\phi^s \rangle$	Geometric mean over the untagged jets

and ϕ moments (M_ϕ) of a jet, which are defined as

$$M_\eta = \sqrt{\left[\sum_{\text{tow}} \frac{E_T^{\text{tow}}}{E_T} \eta_{\text{tow}}^2\right] - \eta^2} \tag{1}$$

and

$$M_\phi = \sqrt{\left[\sum_{\text{tow}} \frac{E_T^{\text{tow}}}{E_T} \phi_{\text{tow}}^2\right] - \phi^2}, \tag{2}$$

where E_T, η, and ϕ are, respectively, the transverse energy, the pseudorapidity, and the azimuthal angle of the jet, while E_T^{tow} is the transverse energy deposited in the calorimeter towers belonging to the jet.

We remove possible biases coming from E_T distributions, which might differ in signal and background events, by deconvoluting the E_T dependence through a rescaling of all moments to a common reference value of $E_T = 50$ GeV. We obtain what we call scaled moments:

$$M_\eta^s = M_\eta \frac{f_q^\eta(50\ \text{GeV})}{f_q^\eta(E_T)} \tag{3}$$

and

$$M_\phi^s = M_\phi \times \frac{f_q^\phi(50\ \text{GeV})}{f_q^\phi(E_T)}, \tag{4}$$

where $f_q^\eta(E_T)$ and $f_q^\phi(E_T)$ are the functions that fit the profiles of M_η vs E_T and of M_ϕ vs E_T in quark-initiated jets from simulated $t\bar{t}$ events.

These scaled moments are quite different for jets coming from a quark or a gluon in simulated $t\bar{t}$ events. Such a behavior has been verified in data events where the jet origin is well known. To take advantage of the large number of jets in a $t\bar{t}$ event, we consider the geometric average of the η moments and of the ϕ moments, see Fig. 1, evaluated using all jets which are not identified as coming from a heavy quark by the criteria explained in Sec. III D.

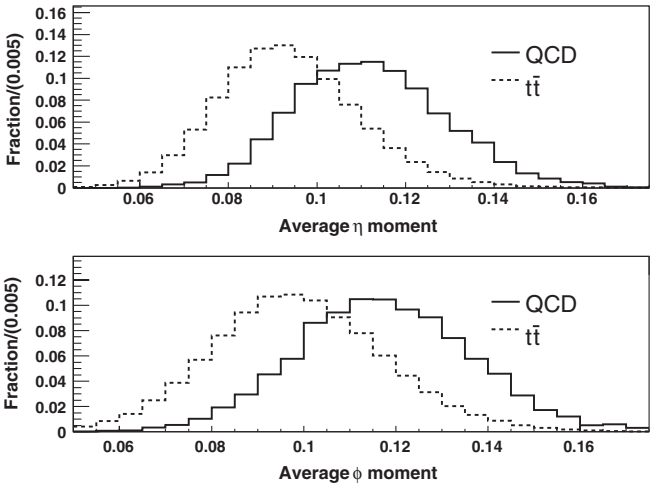

FIG. 1. Geometric average of the η scaled moments ($\langle M_\eta^s \rangle$, upper plot) and of the ϕ scaled moments ($\langle M_\phi^s \rangle$, lower plot) for QCD multijet (solid histogram) and simulated $t\bar{t}$ (dashed histogram) events with $6 \leq N_{\text{jets}} \leq 8$.

The 13 variables are used as inputs to a neural network with two hidden layers with 20 and 10 hidden nodes, respectively, and one output node. The network is trained on same-size samples of signal and background events with $6 \leq N_{\text{jets}} \leq 8$ (about half a million events). In order to model the signal we use the PYTHIA v6.2 [21] leading-order (LO) Monte Carlo generator with parton showering followed by a simulation of the CDF II detector. The reference top quark mass chosen for the training is $M_{\text{top}} = 175\ \text{GeV}/c^2$. The background is obtained from the multijet data events themselves, since the signal fraction is expected to be very small before applying the neural-network selection. The value of the output node, N_{out}, is

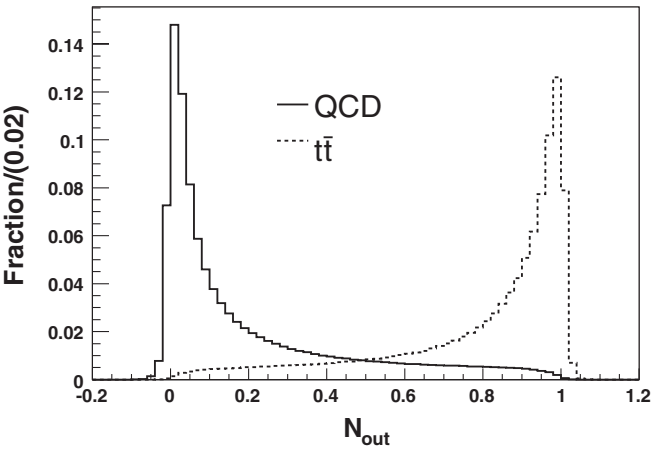

FIG. 2. Neural-network output N_{out} for QCD multijet (solid histogram) and simulated $t\bar{t}$ (dashed histogram) events with $6 \leq N_{\text{jets}} \leq 8$. Histograms are normalized to unity. The neural-network implementation that we use in the *TMultiLayerPerceptron* produces an output which is not strictly bound between 0 and 1.

the quantity we use as a discriminator between signal and background, and is shown in Fig. 2 for the $6 \leq N_{\text{jets}} \leq 8$ sample.

D. Tagging *b* quarks

In order to enrich the $t\bar{t}$ content in the event sample, we use a *b*-tagging algorithm based on secondary vertex reconstruction as described in detail in [14,22]. The algorithm identifies a jet likely to contain a hadron with a *b* quark by reconstructing its decay vertex with at least two high-quality tracks with hits in the silicon vertex detector. A *b*-tagged jet (*tag*, in brief) must have an associated secondary vertex with a displacement from the primary vertex in the transverse plane larger than 7.5 times the transverse-displacement resolution. This is evaluated for each secondary vertex, but its typical value is about 190 μm. The tagging efficiencies for jets coming from the fragmentation of *b* or *c* quarks are corrected in simulated events according to the efficiency seen in the data, by a factor 0.95 ± 0.04, both for *b* jets and *c* jets. These factors are described in detail in [14].

IV. EVENT SIMULATION

The standard model $t\bar{t}$ events used to study the event selection and to check the performance of the method (Sec. IX) are simulated using PYTHIA v6.2 [21]. Samples generated with input values of the top quark mass, $M_{\text{top}}^{\text{in}}$, ranging from 160 to 190 GeV$/c^2$ are considered and, for each sample, the event selection is repeated by varying the JES from its default value [16]. The displacement, denoted as ΔJES, is measured relative to the uncertainty, σ_{JES}, on the default value itself, so that the value of JES applied to simulated events is increased by $\Delta\text{JES} \cdot \sigma_{\text{JES}}$ with respect to the default. To test the method, input values $\Delta\text{JES}^{\text{in}}$ ranging from -3 to $+3$ are considered.

Different generators and different values for the model parameters are used to estimate the systematic uncertainties, as described in Sec. X.

V. BACKGROUND ESTIMATE

The background for the $t\bar{t}$ multijet final state comes mainly from QCD production of heavy-flavor quark pairs ($b\bar{b}$ and $c\bar{c}$) and from false tags of light-flavor quark jets. Other standard model processes such as W/Z + jets have a smaller production cross section and small acceptance due to the selection requirements.

Given the large theoretical uncertainties on the QCD multijet production cross section, a more accurate background estimate is obtained from the data, rather than from Monte Carlo simulations. A tag rate per jet, defined as the probability of tagging a jet whose tracks are reconstructed in the vertex detector (*fiducial* jet), is then evaluated in a sample of events with exactly four jets passing the preselection and therefore still dominated by the background ($\text{S/B} \approx 1/5000$). The rate is parametrized in terms of variables sensitive to both the tagging efficiency for heavy-flavored objects and the probability of false tags: the jet E_T, the number of tracks reconstructed in the silicon vertex detector and associated with the jet, $N_{\text{trk}}^{\text{jet}}$, and the number of primary vertices reconstructed in the event, N_{vert} [4]. By definition, the tag rate estimates the probability that a fiducial jet having, on average, the characteristics of jets from background events is tagged. Its average value is about 3.7%, with negligible uncertainty. However, direct exploitation of the tag rate to predict the number of background events with exactly a given number of tags would give incorrect numbers. This happens because, by construction, this rate is the ratio between the number of tagged jets and the number of fiducial jets in a whole sample of events. Possible correlations among jets in the same event are not considered. As heavy-flavor quarks come in pairs in QCD background, the probability to tag a pair of jets in the same event is therefore larger than the simple product of the tag probabilities of individual jets given by the tag rate.

To account for this we introduce correction factors to obtain a better estimate for the number of 1-tag and $\geq$ 2-tag background events. These factors are derived in a control sample dominated by the background (events with six, seven, or eight jets and $N_{\text{out}} \leq 0.25$, with $\text{S/B} \approx 1/1300$ for one tag and $\text{S/B} \approx 1/400$ for ≥ 2 tags) as the ratio between the observed number of events with *n* tags (with $n = 1, 2, 3$) and the average expectation obtained by using the tag rate to evaluate the probability for each event to have the same number, *n*, of tagged jets. These factors represent, therefore, average corrections to the probability for a possible *tag configuration*, that is, for the assumption that among the fiducial jets in an event of the sample selected before the *b*-tagging requirements (*pretag* sample) only a given subset is actually tagged when the algorithm is applied. Their average values are 0.94, 1.48, and 2.46 for events with one, two, and three tagged jets, with relative statistical uncertainties of 0.4%, 1.1%, and 5.1%, respectively. Similarly to the tag rate, these corrections should be valid for events with the characteristics of background events.

The accuracy of our modeling of the background processes is verified in control samples, i.e. on events with higher values of N_{out} and therefore with a larger fraction of signal events and with possible different kinematics and background composition. As the background prediction is performed using the data in the pretag sample, the presence of $t\bar{t}$ events must also be taken into account. Therefore a correction is applied to derive a better evaluation, $n_{(b,\text{exp})}$, of the background normalization from the raw estimate $n_{(b,\text{raw})}$ directly obtained by the corrected tag rate matrix. This correction must subtract the contribution $n_{t\bar{t}}^{tr}$ coming from applying the matrix to signal events and included in $n_{(b,\text{raw})}$. Denoting by N_{obs} the number of events observed in

the data sample, by $n_{t\bar{t}}$ the number of signal events in this sample, and assuming that the excess of events with respect to the expected background is totally due to the signal, the correction can be written as

$$n_{(b,\mathrm{exp})} = n_{(b,\mathrm{raw})} - n_{t\bar{t}}^{tr} = n_{(b,\mathrm{raw})} - \frac{n_{t\bar{t}}^{tr}}{n_{t\bar{t}}} \cdot n_{t\bar{t}}$$
$$= n_{(b,\mathrm{raw})} - \frac{n_{t\bar{t}}^{tr}}{n_{t\bar{t}}} \cdot (N_{\mathrm{obs}} - n_{(b,\mathrm{exp})}), \quad (5)$$

which, with $R_{t\bar{t}} \equiv n_{t\bar{t}}^{tr}/n_{t\bar{t}}$, gives

$$n_{(b,\mathrm{exp})} = \frac{n_{(b,\mathrm{raw})} - R_{t\bar{t}} \cdot N_{\mathrm{obs}}}{1 - R_{t\bar{t}}}. \quad (6)$$

$R_{t\bar{t}}$ can be inferred from simulated events and amounts to $0.314 \pm 0.003(\mathrm{stat})$ $[0.067 \pm 0.0014(\mathrm{stat})]$ for 1-tag ($\geq$ 2-tag) events. Further possible discrepancies between the observed and expected number of events are considered as due to the modeling of the background and accounted for as a systematic uncertainty.

VI. MASS RECONSTRUCTION

The simultaneous measurement of the top quark mass and the JES is based on the reconstruction, event by event, of both the top quark and the W masses through a constrained fitting technique. The shapes of the distributions obtained by this procedure are sensitive to the values of both M_{top} and JES. Therefore, for simulated events, they are built using samples corresponding to the different input values of M_{top} and ΔJES listed in Sec. IV.

Moreover, given the different resolution in the reconstructed top quark mass and the W-boson mass, and also the different S/B which can be achieved by requiring events with exactly one or ≥ 2 tags, two sets of distributions are separately derived in these samples.

A. Reconstructed top quark mass

For each event we determine a reconstructed top quark mass, m_t^{rec}, from the four-momenta of selected jets. Sixteen equations can be considered to connect the four-momenta of the two top quarks and their decay products according to the $t\bar{t} \rightarrow b\bar{b}W^+W^- \rightarrow b\bar{b}q_1\bar{q}_2q_3\bar{q}_4$ hypothesis:

$$p_t^{\mu} = p_{W^+}^{\mu} + p_b^{\mu}, \quad (7)$$

$$p_{\bar{t}}^{\mu} = p_{W^-}^{\mu} + p_{\bar{b}}^{\mu}, \quad (8)$$

$$p_{W^+}^{\mu} = p_{q_1}^{\mu} + p_{\bar{q}_2}^{\mu}, \quad (9)$$

$$p_{W^-}^{\mu} = p_{q_3}^{\mu} + p_{\bar{q}_4}^{\mu}, \quad (10)$$

with $\mu = 0, 1, 2, 3$. There are 13 unknown quantities, i.e., the unknown top quark mass and the three-momenta of the top quarks and of the W bosons, so the kinematics of the events are overconstrained.

The fit is performed using only the six highest-E_T jets (leading jets) of the event and considering their possible assignments to quarks of a $t\bar{t}$ final state. The total number of different permutations giving two doublets of jets corresponding to the W bosons and two triplets of jets corresponding to the top quarks is 90. Since we require the presence of b tags, assigning the tagged jets only to b quarks reduces this number to 30 for 1-tag events and six in case of two or more b tags [23].

For each permutation the kinematics of the event is reconstructed minimizing the following χ^2 function:

$$\chi^2 = \frac{(m_{jj}^{(1)} - M_W)^2}{\Gamma_W^2} + \frac{(m_{jj}^{(2)} - M_W)^2}{\Gamma_W^2} + \frac{(m_{jjb}^{(1)} - m_t^{\mathrm{rec}})^2}{\Gamma_t^2}$$
$$+ \frac{(m_{jjb}^{(2)} - m_t^{\mathrm{rec}})^2}{\Gamma_t^2} + \sum_{i=1}^{6} \frac{(p_{T,i}^{\mathrm{fit}} - p_{T,i}^{\mathrm{meas}})^2}{\sigma_i^2}. \quad (11)$$

The minimization procedure is performed with respect to seven parameters, i.e., the reconstructed top quark mass m_t^{rec} and the transverse momenta $p_{T,i}^{\mathrm{fit}}$, of the six jets, which are constrained to the measured value $p_{T,i}^{\mathrm{meas}}$ within their known resolution σ_i. The invariant masses of the jet doublets assigned to light-flavor quarks coming from a W, $m_{jj}^{(1,2)}$, and of the trijet systems including one doublet and one of the jets assigned to b quarks, $m_{jjb}^{(1,2)}$, are evaluated by the trial momenta of jets at each step of the minimization. On the contrary, the measured mass M_W and the natural width Γ_W of the W boson as well as the assumed natural width of the top quark, Γ_t, are kept constant to 80.4 GeV/c^2, 2.1 GeV/c^2, and 1.5 GeV/c^2, respectively [24,25].

The permutation of jets which gives the lowest χ^2 value is selected, and the corresponding fitted value of m_t^{rec} enters an invariant mass distribution (*template*) which will be used for the M_{top} measurement.

B. Reconstructed W mass

Reconstructing the mass of W bosons by using dijet systems represents a possibility to obtain a variable, in principle, insensitive to M_{top} which allows, therefore, an independent determination of JES.

To build the m_W^{rec} distributions we use the same procedure and χ^2 expression considered for m_t^{rec}, but now the W-boson mass is also left as a free parameter in the fit (i.e. M_W becomes m_W^{rec}). Again, for each event, the value of m_W^{rec} corresponding to the permutation of the jet-to-parton assignments with the lowest χ^2 enters the distribution.

Using different fits in the reconstruction of m_t^{rec} and m_W^{rec} can lead to selecting different assignments of jets to partons for the two variables in the same event. This is not a problem as the same procedure is followed both on data and simulated events. Reconstructing the top quark mass using a constant value of M_W, as described in Sec. VI A, improves the resolution of the distributions and therefore

the determination of the *true* value of $M_{\rm top}$. The correlations between the values of $m_t^{\rm rec}$ and $m_W^{\rm rec}$ in the same event are taken into account in the calibration of the likelihood fit used for the measurement (Sec. VIII B).

C. Background templates

In order to reconstruct data-driven background templates we apply the kinematical fitter to the sample of events passing the neural-network selection, but before the requirement of tagged b jets.

The same procedures described in Secs. VI A and VI B are repeated on these events assigning fiducial jets to b quarks and then looping over all possible assignments of other jets to the remaining quarks, performing the fit for each permutation and selecting the reconstructed $m_t^{\rm rec}$ and $m_W^{\rm rec}$ values corresponding to the best χ^2. These values then enter the templates weighted by the *corrected* probability of the assumed tag configuration; see Sec. V. As for the normalization, the background distributions also need to be corrected for the presence of signal in the pretag sample by subtracting the contribution from $t\bar{t}$ events. The shape of this contribution is obtained from simulated samples and depends on the assumed $M_{\rm top}$ and JES, while the normalization is given by the difference $n_{(b,\rm raw)} - n_{(b,\rm exp)}$, as described in Sec. V.

In order to check how well our modeling describes the background, we consider events in control regions defined by the $N_{\rm out}$ value, in ranges where the signal presence after tagging is still very low. In these regions the templates, i.e. the main elements of our measurement, are reconstructed by the procedure described in the previous sections, both for the signal and the background, as well as other important distributions like $N_{\rm out}$ and the χ^2 of the fit used to build the $m_t^{\rm rec}$ templates. These distributions are then compared to observed data, taking into account the contribution from signal events. The agreement is generally good in all the control regions, and this confirms the reliability of the background model.

Figures 3 and 4 show, as examples, distributions of $m_t^{\rm rec}$ and $m_W^{\rm rec}$ in one of the control regions for 1-tag and $\geq$ 2-tag events, where the sum of signal and background is compared to the same distributions reconstructed in the data. In these plots the integral of the signal distributions corresponding to $M_{\rm top} = 175\ {\rm GeV}/c^2$ and the default value $\Delta{\rm JES} = 0$ have been normalized to the difference between the observed data and the corrected expected background.

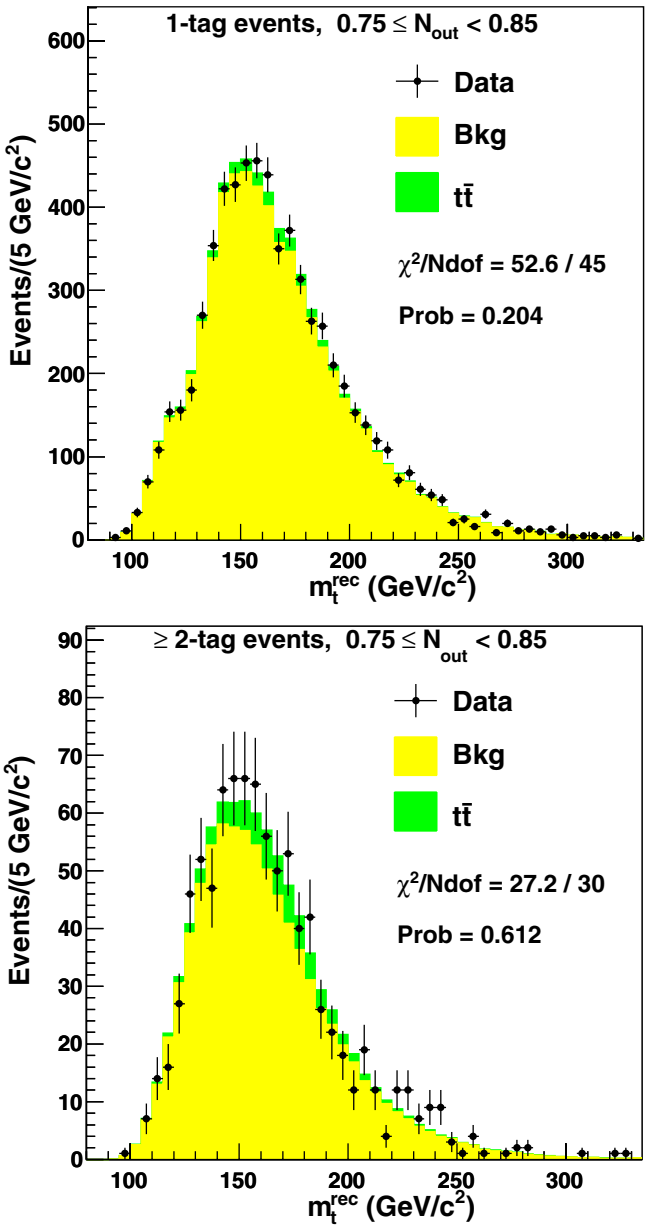

FIG. 3 (color online). Histograms of the reconstructed top quark mass $m_t^{\rm rec}$ for 1-tag events, upper plot, and $\geq$ 2-tag events, lower plot, are shown in a control region defined by $0.75 \leq N_{\rm out} < 0.85$. Along with the data are plotted the expected background and the signal contribution for $M_{\rm top} = 175\ {\rm GeV}/c^2$ and the default value $\Delta{\rm JES} = 0$, normalized to the difference between the data and the background. The value of the purely statistical χ^2 probability is reported on each plot.

VII. EVENT SAMPLES

In order to obtain the best performance from our method, we performed sets of *pseudoexperiments* (PEs) to find out which requirements on the values of $N_{\rm out}$ and of the χ^2 used to obtain the $m_t^{\rm rec}$ values minimize the statistical uncertainty on the top quark mass measurement. The procedure is similar to the one outlined in Sec. IX, with a binned version of the same likelihood. It is applied separately to 1-tag and $\geq$ 2-tag samples and considers many different combinations of possible requirements. The smallest values for the uncertainty are obtained using ($N_{\rm out} \geq 0.90$, $\chi^2 \leq 6$) in the 1-tag sample and ($N_{\rm out} \geq 0.88$, $\chi^2 \leq 5$) in the $\geq$ 2-tag sample so that we add these requirements to the prerequisites described in Sec. III B.

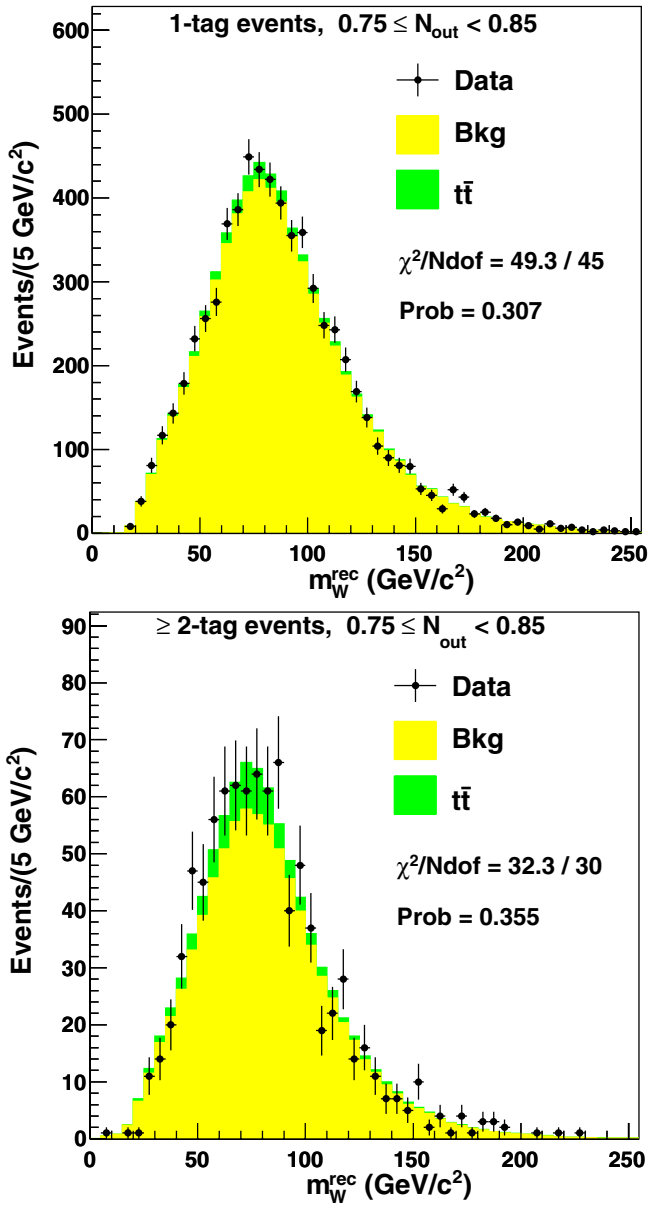

FIG. 4 (color online). Histograms of the reconstructed W mass m_W^{rec} for 1-tag events, upper plot, and $\geq$ 2-tag events, lower plot, are shown in a control region defined by $0.75 \leq N_{\mathrm{out}} < 0.85$. Along with the data are plotted the expected background and the signal contribution for $M_{\mathrm{top}} = 175\ \mathrm{GeV}/c^2$ and the default value $\Delta\mathrm{JES} = 0$, normalized to the difference between the data and the background. The value of the purely statistical χ^2 probability is reported on each plot.

The final definition of the samples used in our analysis is summarized in Table II.

After these selections, 3452 and 441 events are observed for the 1-tag and $\geq$ 2-tag samples, respectively. We can evaluate the average number of background events expected in the selected samples and their uncertainties, as described in Sec. V. The systematic uncertainties on the background normalizations are estimated by assuming that the discrepancy between the observed number of events in the data and the sum of the expected contributions from signal and background (where, in this case, the theoretical cross section value of 6.7 pb is considered for $t\bar{t}$ events production) is due to a bad evaluation of the background. This is done separately for 1-tag and $\geq$ 2-tag samples, and the resulting relative uncertainties on the expected number of events are $\sigma(n_{(b,\mathrm{exp})}^{1\ \mathrm{tag}}) = 2.9\%$ and $\sigma(n_{(b,\mathrm{exp})}^{\geq 2\ \mathrm{tags}}) = 14.6\%$, respectively. The efficiencies of the full selection on $t\bar{t}$ events corresponding to $M_{\mathrm{top}} = 175\ \mathrm{GeV}/c^2$ and $\Delta\mathrm{JES} = 0$ are 3.6% and 1.0% for 1-tag and $\geq$ 2-tag events, respectively. These values are used to evaluate the expected signal contributions of Table III, where $\sigma_{t\bar{t}} = 6.7$ pb is assumed. In the same table, the observed number of events and the expected background in each sample are also summarized.

TABLE II. Final definition and requirements for selected event samples.

Event sample	b tags	N_{out}	m_t^{rec} fit χ^2
One tag	$\equiv 1$	≥ 0.90	≤ 6
≥ 2 tags	2 or 3	≥ 0.88	≤ 5

TABLE III. Number of events observed in the selected data samples and corresponding expected numbers of background and $t\bar{t}$ events. The signal contribution is evaluated for $M_{\mathrm{top}} = 175\ \mathrm{GeV}/c^2$, $\Delta\mathrm{JES} = 0$, and $\sigma_{t\bar{t}} = 6.7$ pb.

Event sample	Observed	Background	$t\bar{t}$
One tag	3452	2785 ± 83	693
≥ 2 tags	441	201 ± 29	193

VIII. LIKELIHOOD FIT

The technique described in Sec. VI allows one to obtain sets of *observed* m_t^{rec} and m_W^{rec} values reconstructed in the data samples with 1 or $\geq$ 2 tags as well as to build signal and background distributions for the same variables. In order to measure the top quark mass simultaneously with the JES, a fit is performed where an unbinned likelihood function is maximized to find the values of M_{top}, $\Delta\mathrm{JES}$, and the number of signal (n_s) and background (n_b) events for each tagging category which give the probability density functions (p.d.f.'s) best describing the data.

A. Probability density functions

The signal templates are fitted by normalized combinations of Gamma and Gaussian p.d.f.'s, and the dependence of the shape on input M_{top} and $\Delta\mathrm{JES}$ is included, writing the parameters of the p.d.f.'s as linear functions of these

variables. Figures 5 and 6 show examples of the fitted p.d.f.'s superimposed on the $m_t^{\rm rec}$ and $m_W^{\rm rec}$ signal templates, respectively, for different $M_{\rm top}$ and ΔJES values.

The shape of distributions built for the background cannot depend on the characteristics of signal events, and, in particular, on the value of top quark mass. Moreover, as they are obtained from data, the shapes correspond to the reference value of the jet energy scale. For these reasons no dependence on $M_{\rm top}$ and JES is considered in the p.d.f.'s used to fit the background templates. Actually, a very weak dependence is introduced through the corrections to the shape of the background distributions, performed to take into account the presence of signal events in the pretag sample, as described in Sec. VI C. These effects are taken into account as a systematic uncertainty. Examples of background $m_t^{\rm rec}$ and $m_W^{\rm rec}$ distributions and the corresponding fitted p.d.f.'s are shown in Fig. 7 for $\geq$ 2-tag events. Discrepancies between the fitted p.d.f.'s and the corresponding distributions are considered in the calibration procedure, presented in Sec. IX.

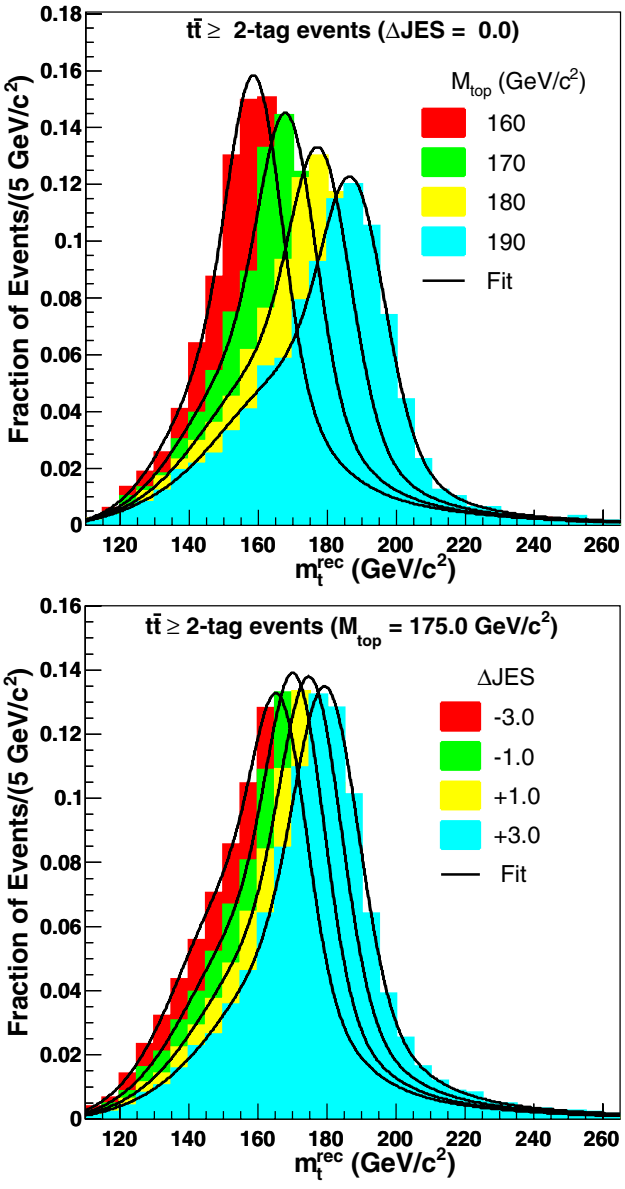

FIG. 5 (color online). Histograms and corresponding fitted probability density functions for the signal $m_t^{\rm rec}$ in $\geq$ 2-tag events for a constant ΔJES value (ΔJES = 0), varying the input top quark mass (upper plot), and for a constant $M_{\rm top}$ value (175 GeV/c^2), varying the input jet energy scale (lower plot).

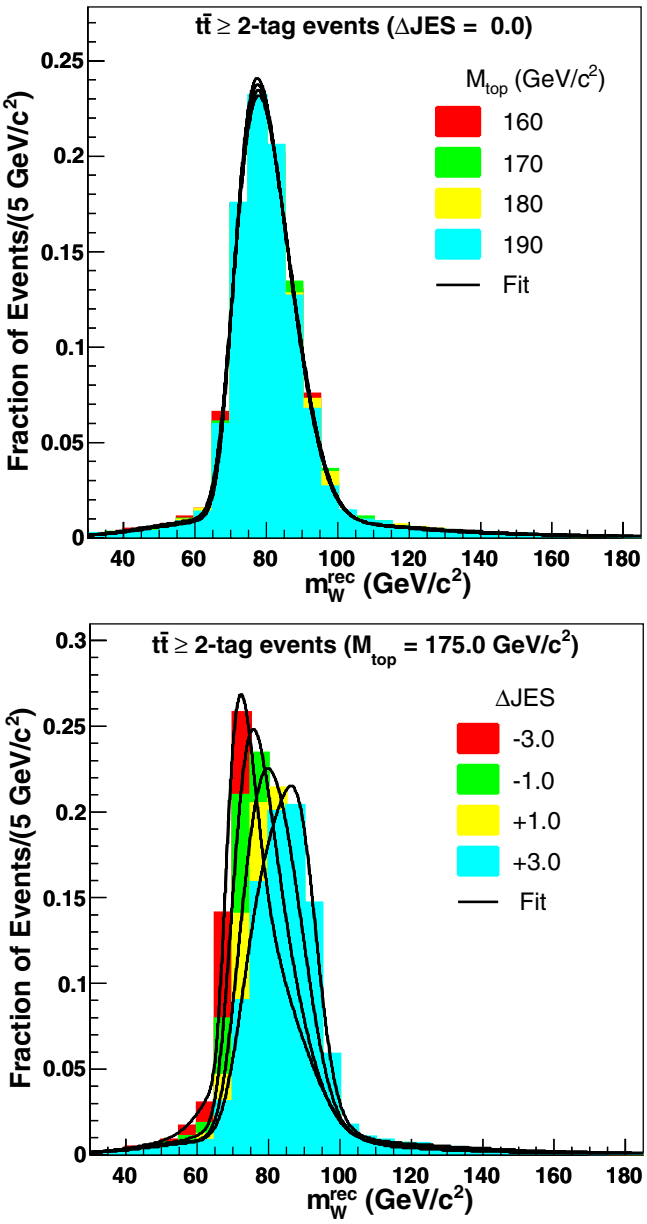

FIG. 6 (color online). Histograms and corresponding fitted probability density functions for the signal $m_W^{\rm rec}$ in $\geq$ 2-tag events for a constant ΔJES value (ΔJES = 0), varying the input top quark mass (upper plot), where the independence of $m_W^{\rm rec}$ on $M_{\rm top}$ is apparent, and for a constant $M_{\rm top}$ value (175 GeV/c^2), varying the input jet energy scale (lower plot).

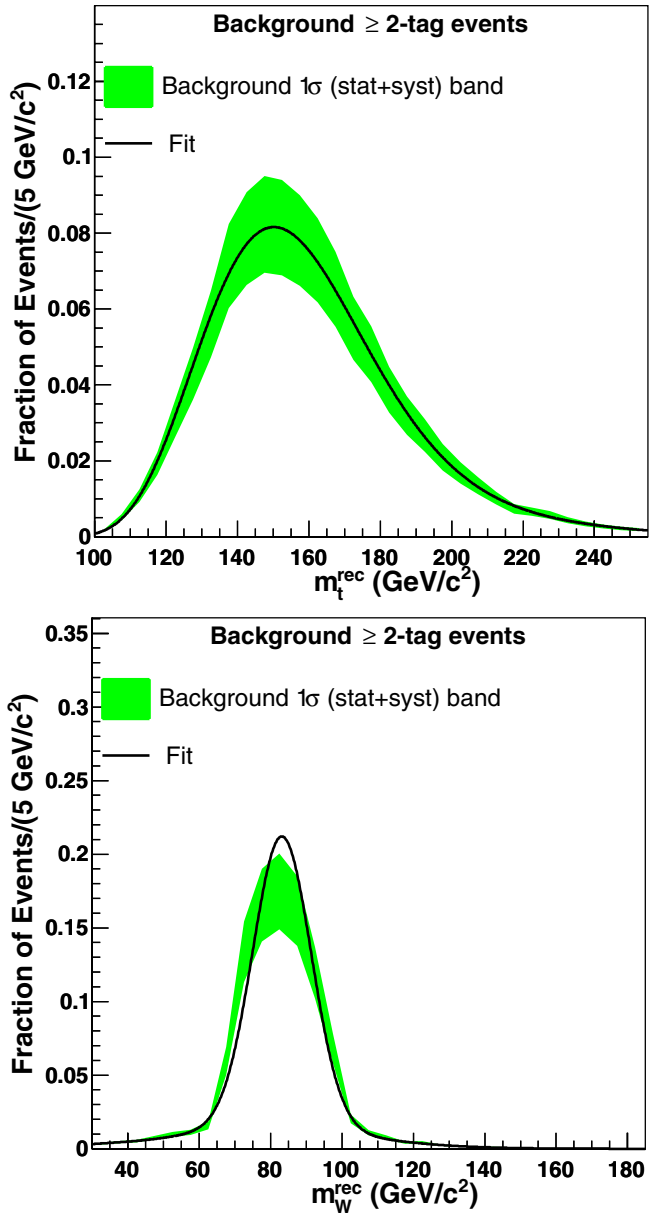

FIG. 7 (color online). Data-driven background histograms of m_t^{rec} (upper plot) and m_W^{rec} (lower plot) for $\geq$ 2-tag events. The bands denote the 1σ uncertainty on the bin contents of the histograms, including both statistical and systematic contributions. The solid lines show the p.d.f.'s fitted to the histograms.

B. The likelihood function

The likelihood function $\mathcal{L}$ is divided into three main parts and can be written as

$$\mathcal{L} = \mathcal{L}_{1\text{ tag}} \times \mathcal{L}_{\geq 2\text{ tags}} \times \mathcal{L}_{\Delta\mathrm{JES}_{\mathrm{constr}}}. \quad (12)$$

The $\mathcal{L}_1$ and $\mathcal{L}_{\geq 2\text{ tags}}$ terms further consist of other factors:

$$\mathcal{L}_{1,\geq 2\text{ tags}} = \mathcal{L}_{M_{\mathrm{top}}} \times \mathcal{L}_{\mathrm{JES}} \times \mathcal{L}_{\mathrm{Poiss}} \times \mathcal{L}_{N_{\mathrm{constr}}^{\mathrm{bkg}}}, \quad (13)$$

where the four terms on the right side assume, respectively, the following form [the superscripts referring to the tag sample are omitted and $f_s \equiv n_s/(n_s + n_b)$, $f_b \equiv 1 - f_s$]:

$$\prod_{i=1}^{N_{\mathrm{obs}}} f_s \cdot P_{\mathrm{sig}}^{m_t^{\mathrm{rec}}}(m_{t,i}|M_{\mathrm{top}}, \Delta\mathrm{JES}) + f_b \cdot P_{\mathrm{bkg}}^{m_t^{\mathrm{rec}}}(m_{t,i}), \quad (14)$$

$$\prod_{i=1}^{N_{\mathrm{obs}}} f_s \cdot P_{\mathrm{sig}}^{m_W^{\mathrm{rec}}}(m_{W,i}|M_{\mathrm{top}}, \Delta\mathrm{JES}) + f_b \cdot P_{\mathrm{bkg}}^{m_W^{\mathrm{rec}}}(m_{W,i}), \quad (15)$$

$$\frac{e^{-(n_s+n_b)} \cdot (n_s + n_b)^{N_{\mathrm{obs}}}}{N_{\mathrm{obs}}!}, \quad (16)$$

$$\exp\left[-\frac{(n_b - n_{(b,\mathrm{exp})})^2}{2\sigma^2_{n_{(b,\mathrm{exp})}}}\right]. \quad (17)$$

In expression (14) the probability to observe the set $m_{t,i}$, $(i = 1, \ldots, N_{\mathrm{obs}})$ of m_t^{rec} values reconstructed in the data is calculated by using the total probability density function resulting from the combination of the parametrized signal and background p.d.f.'s (Sec. VIII A), $P_{\mathrm{sig}}^{m_t^{\mathrm{rec}}}$ and $P_{\mathrm{bkg}}^{m_t^{\mathrm{rec}}}$, respectively, as a function of the free parameters of the fit. In term (15) the same is done for the set of the observed W masses, $m_{W,i}$, $(i = 1, \ldots, N_{\mathrm{obs}})$, and the m_W^{rec} p.d.f. The term (16), $\mathcal{L}_{\mathrm{Poiss}}$, gives the probability to observe the number of events selected in the data, given the average number of signal (n_s) and background (n_b) events expected in the sample, as assumed at each step of the likelihood fit. In the last term, (17), the parameter n_b is constrained by a Gaussian to the *a priori* background estimate given in Sec. VII, i.e. $n_{(b,\mathrm{exp})} = 2785 \pm 83$ for 1-tag events and $n_{(b,\mathrm{exp})} = 201 \pm 29$ for $\geq$ 2-tag events. Finally, the last term in expression (12), $\mathcal{L}_{\Delta\mathrm{JES}_{\mathrm{constr}}}$, is a Gaussian term constraining ΔJES to its *a priori* value:

$$\exp\left[-\frac{(\Delta\mathrm{JES} - \Delta\mathrm{JES}_{\mathrm{constr}})^2}{2}\right]. \quad (18)$$

When the measurement is performed on data, the JES can be constrained to the value independently measured in [16]. Given the meaning of ΔJES, described in Sec. IV, this means that, in this case, $\Delta\mathrm{JES}_{\mathrm{constr}} = 0$.

IX. VERIFICATION AND CALIBRATION OF THE METHOD

We want to investigate the possible presence of biases in the top quark mass and jet energy scale measurements introduced by our method, as well as to have an estimate of its statistical power before performing the measurement on the actual data sample. To do so, we run realistic PEs where *pseudodata* are extracted from simulated signal and data-driven background distributions. A set of 3000 PEs is performed for each simulated value of the top quark mass and of the displacement in the jet energy scale (Sec. IV).

Using the notation introduced in Sec. IV, we refer to these input values as $M_{\rm top}^{\rm in}$ and $\Delta{\rm JES}^{\rm in}$, and they represent the *true* values we want to measure. In each PE the actual numbers of signal ($N_{(s,{\rm obs})}$) and background ($N_{(b,{\rm obs})}$) events in each tagging category are generated with Poisson distributions with mean $n_{(s,{\rm exp})} = N_{\rm obs} - n_{(b,{\rm exp})}$ and $n_{(b,{\rm exp})}$, respectively, where $N_{\rm obs}$ are the observed number of events in the data samples ($N_{\rm obs} = 3452$ for 1-tag and $N_{\rm obs} = 441$ for $\geq$ 2-tag events). A set of $N_{(s,{\rm obs})}$ and $N_{(b,{\rm obs})}$ mass values is then drawn from $m_t^{\rm rec}$ and $m_W^{\rm rec}$ distributions of signal and background and used as input to the likelihood fit (Sec. VIII) that returns simultaneous measurements of $M_{\rm top}$ and ΔJES, denoted as $M_{\rm top}^{\rm out}$ and $\Delta{\rm JES}^{\rm out}$. The average of these measurements over the whole set of 3000 PEs represents the best estimate of the input values obtained by the fitting procedure and therefore can be used to study its behavior. We fit the dependence of these averages with respect to the input values over the whole range of simulated $M_{\rm top}^{\rm in}$ and $\Delta{\rm JES}^{\rm in}$ as

$$\langle M_{\rm top}^{\rm out}\rangle = (A_{00} + A_{01}\cdot\Delta{\rm JES}^{\rm in}) + (A_{10} + A_{11}\cdot\Delta{\rm JES}^{\rm in})\cdot(M_{\rm top}^{\rm in} - 175), \quad (19)$$

$$\langle\Delta{\rm JES}^{\rm out}\rangle = [B_{00} + B_{01}\cdot(M_{\rm top}^{\rm in} - 175)] + [B_{10} + B_{11}\cdot(M_{\rm top}^{\rm in} - 175)]\cdot\Delta{\rm JES}^{\rm in}. \quad (20)$$

These relations can be inverted to obtain calibration functions to be applied to further measurements and therefore, on average, a more reliable estimate of the true values (2D calibration). The calibrated values resulting from a measurement giving $M_{\rm top}^{\rm out}$ and $\Delta{\rm JES}^{\rm out}$ are denoted as $M_{\rm top}^{\rm corr}$ and $\Delta{\rm JES}^{\rm corr}$, while the respective uncertainties, obtained by propagating through the calibration the uncertainties from the likelihood fit, are $\delta M_{\rm top}^{\rm corr}$ and $\delta\Delta{\rm JES}^{\rm corr}$. A second set of PEs is then performed to test the goodness of the procedure. Table IV shows the coefficients A_{ij} and B_{ij} obtained both from calibrated and uncalibrated PEs compared to their ideal values in the absence of any bias.

In Fig. 8 examples of linearity plots are shown for calibrated PEs. These plots, together with the numbers in Table IV, show how the calibration removes any average bias. To check that the uncertainties $\delta M_{\rm top}^{\rm corr}$ and $\delta\Delta{\rm JES}^{\rm corr}$ are also unbiased, we consider the width of $M_{\rm top}^{\rm corr}$ and $\Delta{\rm JES}^{\rm corr}$ pull distributions, that is, the distributions of deviations of the calibrated values from the true inputs in the PEs, divided by the uncertainties themselves. We find that the uncertainties are both underestimated, and multiplicative correction factors equal to 1.084 for $\delta M_{\rm top}^{\rm corr}$ and to 1.115 for $\delta\Delta{\rm JES}^{\rm corr}$ are needed. After these corrections the

TABLE IV. Coefficients of expressions (19) and (20) as obtained from calibrated and uncalibrated pseudoexperiments. The ideal values in the absence of any bias are also shown.

	Uncalibrated PEs	Calibrated PEs	Ideal value
A_{00}	175.47 ± 0.01	174.99 ± 0.01	175
A_{01}	-0.24 ± 0.01	0.00 ± 0.01	0
A_{10}	0.985 ± 0.002	1.000 ± 0.002	1
A_{11}	0.009 ± 0.001	0.000 ± 0.001	0
B_{00}	-0.026 ± 0.003	0.002 ± 0.003	0
B_{01}	0.0009 ± 0.0004	-0.0001 ± 0.0004	0
B_{10}	1.052 ± 0.002	0.999 ± 0.002	1
B_{11}	-0.0016 ± 0.0002	0.0001 ± 0.0002	0

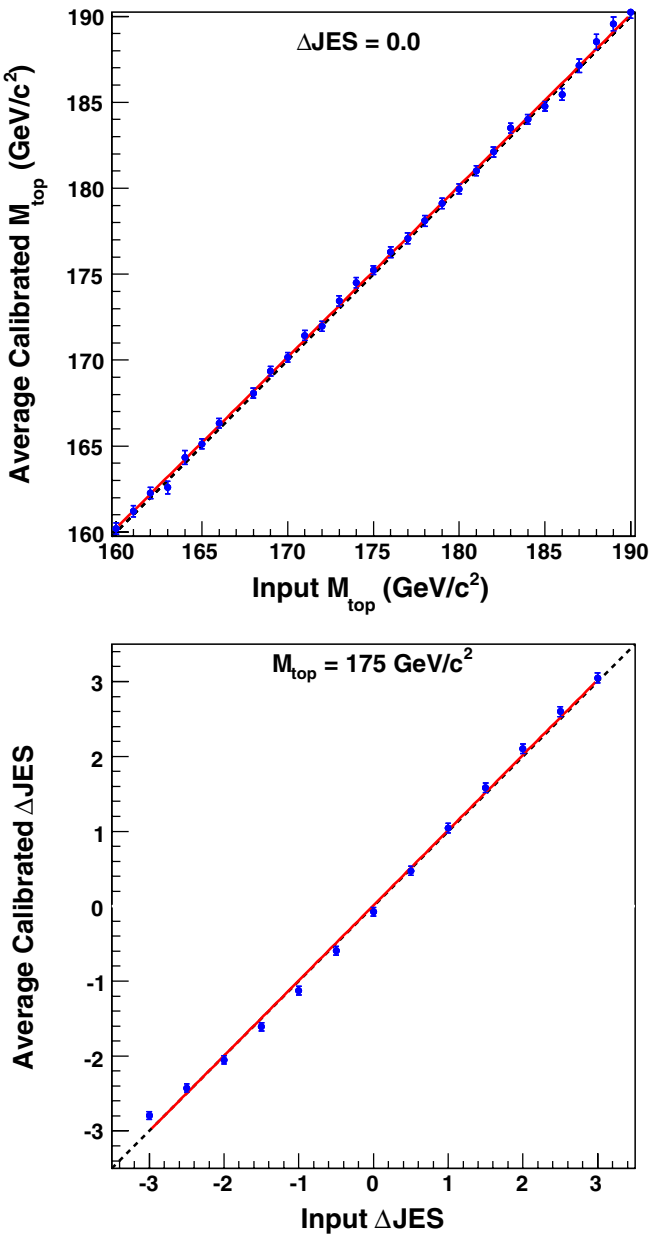

FIG. 8 (color online). Examples of response linearity plots ($\langle M_{\rm top}^{\rm corr}\rangle$ vs $M_{\rm top}^{\rm in}$, upper plot, and $\langle\Delta{\rm JES}^{\rm corr}\rangle$ vs $\Delta{\rm JES}^{\rm in}$, lower plot) after the 2D calibration. The solid lines represent the linear functions which best fit the response as a function of the input values, while the dashed lines represent the ideal behavior.

average expected uncertainty on the measured top quark mass and jet energy scale displacement for true $M_{\rm top}$ and ΔJES around 175 GeV/c^2 and 0 are

$$\delta M_{\rm top}^{\rm corr}({\rm stat} + {\rm JES}) = 2.0\ {\rm GeV}/c^2, \quad (21)$$

$$\delta\Delta{\rm JES}^{\rm corr}({\rm stat} + M_{\rm top}) = 0.45. \quad (22)$$

X. SYSTEMATIC UNCERTAINTIES

The possible systematic uncertainties on the top quark mass and the jet energy scale measurements have been studied and are summarized in this section. These arise mostly from the measurement technique itself, from uncertainties in the simulation of the $t\bar{t}$ events, from mismodeling of the detector response, and from uncertainty on the shapes of signal and background templates used to derive the p.d.f.'s and to calibrate the measurement. The uncertainties are usually evaluated by performing PEs, extracting pseudodata from templates built using signal samples where the possible systematic effects have been considered and included. Corrections to the shape of the raw background templates are performed as described in Sec. VI C to obtain the corrected background templates corresponding to the effect one wants to study. On the contrary, nothing is changed in the elements of the likelihood fit, because it is the default procedure that we want to apply to real data and that, therefore, we have to test in case of possible mismodeling of the data themselves. The results from these PEs are then compared to the ones obtained by using default templates, and the shifts in the average $M_{\rm top}^{\rm corr}$ and $\Delta{\rm JES}^{\rm corr}$ values are taken as the estimate of the systematic uncertainties. In some cases the statistical uncertainties on the shifts may be larger than the shifts themselves, and therefore we use conservatively the former as the systematic uncertainty. In the following, after the description of each effect, we also quote in parentheses the values of the corresponding uncertainties for the top quark mass and the jet energy scale, respectively. These values are then summarized in Table V.

The 2D calibration removes the average biases, especially related to the parametrization of the templates using smooth probability density functions. Residual biases usually exist at single ($M_{\rm top}^{\rm in}$, $\Delta{\rm JES}^{\rm in}$) points, and have to be taken into account. We therefore consider the shift of the mean of the pull distributions with respect to 0 at each ($M_{\rm top}^{\rm in}$, $\Delta{\rm JES}^{\rm in}$) point to evaluate this *residual bias* systematic uncertainty, which, given the definition of pull in Sec. IX, is defined as a function of the uncertainty on the calibrated measurements. To obtain the proper coverage of both positive and negative biases we evaluate them separately, so that asymmetric uncertainties are finally considered. They are generally given by $(^{+0.37}_{-0.20}) \cdot \delta M_{\rm top}^{\rm corr}$ for $M_{\rm top}^{\rm corr}$ and $(^{+0.43}_{-0.56}) \cdot \delta\Delta{\rm JES}^{\rm corr}$ for $\Delta{\rm JES}^{\rm corr}$. Specifying the values obtained in the measurement on the data, described in Sec. XI, we obtain $^{+0.8}_{-0.4}$ GeV/c^2 on $M_{\rm top}^{\rm corr}$, $^{+0.18}_{-0.24}$ on $\Delta{\rm JES}^{\rm corr}$.

TABLE V. Systematic uncertainties and their sizes for the top quark mass and the jet energy scale measurements. The total uncertainty is obtained by the sum in quadrature of single contributions.

Source	$\delta M_{\rm top}^{\rm syst}$ (GeV/c^2)	$\delta\Delta{\rm JES}^{\rm syst}$
Residual bias	$^{+0.8}_{-0.4}$	$^{+0.18}_{-0.24}$
2D calibration	<0.1	<0.01
Generator	0.3	0.25
ISR/FSR	0.1	0.06
b-jet energy scale	0.2	0.04
b-tag SF E_T dependence	0.1	0.01
Residual JES	0.5	...
PDF	$^{+0.3}_{-0.2}$	$^{+0.05}_{-0.04}$
Multiple $p\bar{p}$ interactions	0.2	0.01
Color reconnection	0.4	0.08
Statistics of templates	0.3	0.07
Background shape	0.1	0.02
Total	$^{+1.2}_{-1.0}$	$^{+0.34}_{-0.37}$

The uncertainties on the parameters of the 2D calibration give a small uncertainty on the corrected values $M_{\rm top}^{\rm corr}$ and $\Delta{\rm JES}^{\rm corr}$ which can be evaluated by the calibration functions and the values of $M_{\rm top}$ and ΔJES fitted in the data (< 0.1 GeV/c^2, <0.01).

Many sources of systematic effects arise from uncertainties in modeling of the hard interaction in simulated events. PYTHIA and HERWIG [26] Monte Carlo generators differ in their hadronization schemes and in their description of the underlying event and multiple interactions. The default signal samples have been generated with PYTHIA, and therefore an uncertainty is obtained by using a sample generated using HERWIG (0.3 GeV/c^2, 0.25).

Jets coming from possible emission of hard gluons might fall among the six leading jets and populate the tails in the top quark invariant mass distribution. The amount of radiation from partons in the initial or final state is set by parameters of the PYTHIA generator used to simulate signal events. To study these effects, templates are built using samples where the values of the parameters have been changed with respect to the default, to increase or to decrease the amount of radiation [22] (0.1 GeV/c^2, 0.06).

Since the default jet energy corrections are derived from data samples deficient in heavy flavors [16], an additional uncertainty comes from considering the different properties of b quarks. We account for the uncertainties on the b-quark semileptonic branching ratios, fragmentation modeling, and calorimeter response to heavy-flavor hadrons (0.2 GeV/c^2, 0.04).

The different efficiency of the b-tagging algorithm on data and simulated events is usually considered by introducing a constant scale factor (b-tag SF). The overall

uncertainty on this parameter affects the cross section measurement described in Sec. XII. However, such a scale factor does not need to be considered regarding the top quark mass measurement, because it could slightly change only the population of the signal templates but not their shape. On the other hand, variations of the latter could be caused by the possible dependence of the b-tag SF on the transverse energy of jets, which is then considered as a systematic effect (0.1 GeV/c^2, 0.01).

The uncertainty on the top quark mass coming from the likelihood fit includes the uncertainty due to the jet energy scale. However, as described in Sec. III B, this uncertainty is the result of many independent effects with different behavior with respect to properties of jets like E_T and η [16], and therefore represents a leading-order correction. Second-order effects can arise from uncertainties on the single corrections applied to the jet energies. To evaluate these possible effects, we build signal templates by varying separately by $\pm 1\sigma$ the single corrections and, for each one of these variations, PEs were performed by using these templates and not applying the constraint $\mathcal{L}_{\Delta\mathrm{JES}_{\mathrm{constr}}}$ in the likelihood fit, as this term is related to effects of the full correction. The resulting uncertainties have been added in quadrature to obtain a *residual* JES uncertainty on the top quark mass (0.5 GeV/c^2).

The choice of parton distribution functions (PDF) in the proton used in Monte Carlo generators can affect the kinematics of simulated $t\bar{t}$ events and thus the top quark mass measurement. We considered four sources of uncertainties: the difference arising from the use of the default CTEQ5L [27] PDF and one calculated from the MRST group, MRST72 [28]; the uncertainty depending on the value of α_s, evaluated by the difference between the use of MRST72 and MRST75 PDF's; the uncertainty depending on the differences between the LO and NLO calculations of PDF's, evaluated by the difference between using default CTEQ5L (LO) and CTEQ6M (NLO) PDF's; and the uncertainties on PDF's derived from experimental data uncertainties ($^{+0.3}_{-0.2}$ GeV/c^2, $^{+0.05}_{-0.04}$).

The probability to have multiple $p\bar{p}$ interactions during the same bunch crossing is a function of the instantaneous luminosity. This is reflected in the increasing number of primary vertices reconstructed in the events at higher luminosities. We account for the fact that the simulated samples for the signal process do not model the actual luminosity profile of the data by considering the signal distributions for events with 1, 2, 3, and ≥ 4 reconstructed vertices separately. These distributions are then used to obtain the templates by weighted averages, where the weights are evaluated as the fractions of events with 1, 2, 3, and ≥ 4 vertices observed in the data. Moreover, a possible mismodeling of the dependence of the jet energy response as a function of the reconstructed number of primary vertices in simulated events is considered (0.2 GeV/c^2, 0.01).

Uncertainties from modeling of color reconnection effects [29] are estimated by comparing the results of two sets of PEs performed drawing pseudodata from templates built using two different samples of events simulated by PYTHIA. The samples are generated with two different sets of parameters, corresponding to two different models of color reconnection (0.4 GeV/c^2, 0.08).

The shapes of the signal and background distributions are affected by uncertainties due to the limited statistics of the simulated events and data samples used to build them. These uncertainties affect the results of a measurement which is performed maximizing an unbinned likelihood where parametrized p.d.f.'s, fitted to default templates, are evaluated. We address this effect, obtaining 100 sets of templates by statistical fluctuations of default ones and performing pseudoexperiments drawing data from each of these sets separately. From each set we obtain an average value for $M_{\mathrm{top}}^{\mathrm{corr}}$ and $\Delta\mathrm{JES}^{\mathrm{corr}}$, and the spread of these values is taken as the systematic uncertainty (0.3 GeV/c^2, 0.07).

Besides the purely statistical effects, quoted above, the shape of the background templates also has uncertainties due to the corrections for the presence of signal events in the pretag sample, Sec. VI C, and to the systematic uncertainty on the background normalization, Sec. VII. We address this source of systematic uncertainty by the same technique used for the statistical contributions, that is, by obtaining a set of 100 background templates where the content of each bin is separately fluctuated by Gaussian distributions centered on the default bin content and with a width equal to its systematic uncertainty, and taking the spread of results from PEs as the systematic uncertainty (0.1 GeV/c^2, 0.02).

Table V shows a summary of all the systematic uncertainties and their sum in quadrature, which gives a total systematic uncertainty of $^{+1.2}_{-1.0}$ GeV/c^2 for the M_{top} measurement and $^{+0.34}_{-0.37}$ for the ΔJES.

XI. TOP MASS AND JES MEASUREMENTS

After the kinematical selection with $N_{\mathrm{out}} \geq 0.90$ (≥ 0.88) and $\chi^2 \leq 6$ (≤ 5), we are left with 3452 (441) events with one (≥ 2) tag(s). The background amounts to 2785 ± 83 (201 ± 29) for events with one (≥ 2) tag(s).

For these events a top quark mass has been reconstructed using the likelihood fit described in Sec. VIII B and applied to the data sample. Once the calibration procedure and corrections are applied, as described in Sec. IX, the best estimate of the top quark mass is

$$M_{\mathrm{top}} = 174.8 \pm 2.4(\mathrm{stat} + \mathrm{JES})\ \mathrm{GeV}/c^2, \qquad (23)$$

while the value obtained for the jet energy scale displacement is

$$\Delta\mathrm{JES} = -0.30 \pm 0.47(\mathrm{stat} + M_{\mathrm{top}}). \qquad (24)$$

We can also evaluate separately the purely statistical contributions, obtaining

$$M_{\text{top}} = 174.8 \pm 1.7(\text{stat}) \pm 1.6(\text{JES})\ \text{GeV}/c^2 \quad (25)$$

and

$$\Delta\text{JES} = -0.30 \pm 0.35(\text{stat}) \pm 0.32(M_{\text{top}}). \quad (26)$$

The plot in Fig. 9 shows the measured values together with the log-likelihood contours corresponding to 1σ, 2σ, and 3σ uncertainty on the value of the top quark mass [24]. The slope of the major axis of the contours denotes that the measurements of M_{top} and ΔJES have a negative correlation, and the value of the correlation coefficient obtained from the likelihood fit is -0.68.

The plots in Fig. 10 show the m_t^{rec} distributions for the data compared to the expected background and the signal for a top quark mass of 175.0 GeV/c^2 and a jet energy scale displacement of -0.3, that is, the values of simulated M_{top} and ΔJES as close as possible to the measurements in the data. The signal and background contributions are normalized to the respective number of events as fitted in the data.

The plots in Fig. 11 compare the measured statistical uncertainty, just after the 2D calibration, with the expected distribution from default pseudoexperiments using as inputs $M_{\text{top}} = 175.0$ GeV/c^2 and $\Delta\text{JES} = -0.3$. We find

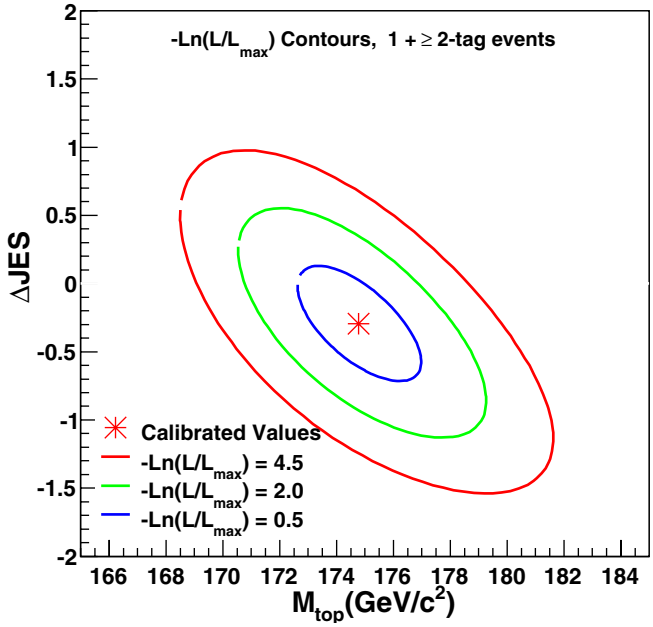

FIG. 9 (color online). Negative log-likelihood contours for the likelihood fit performed for the M_{top} and ΔJES measurements. The minimum is also shown and corresponds to the values measured in the data. The contours are drawn at values of 0.5, 2.0, and 4.5 of the increase of the log-likelihood from the minimum value. These curves correspond to 1σ, 2σ, and 3σ uncertainty on the measurement of the top quark mass.

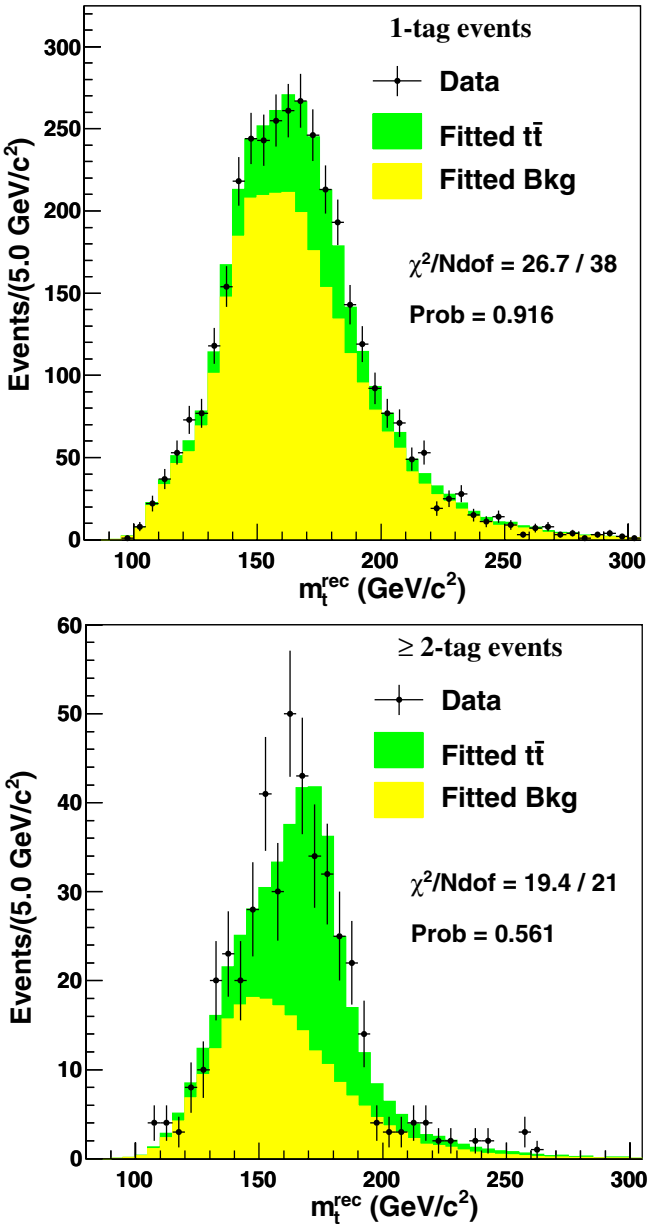

FIG. 10 (color online). Histograms of m_t^{rec} as obtained in the data (black points) for 1-tag (upper plot) and $\geq$ 2-tag events (lower plot) are compared to the distributions from signal and background corresponding to $M_{\text{top}} = 175$ GeV/c^2 and $\Delta\text{JES} = -0.3$. The expected histograms are normalized to the measured values for the average number of signal and background events. The values of the purely statistical χ^2 and of its probability are reported on each plot, showing the overall agreement between the data and the distributions corresponding to the fitted values of M_{top} and ΔJES.

that the probability of achieving a better sensitivity is 91.6% for M_{top} and 81.2% for ΔJES.

Summarizing, the measured values for the top quark mass and the jet energy scale are

$$M_{\text{top}} = 174.8 \pm 2.4(\text{stat} + \text{JES})^{+1.2}_{-1.0}(\text{syst})\ \text{GeV}/c^2, \quad (27)$$

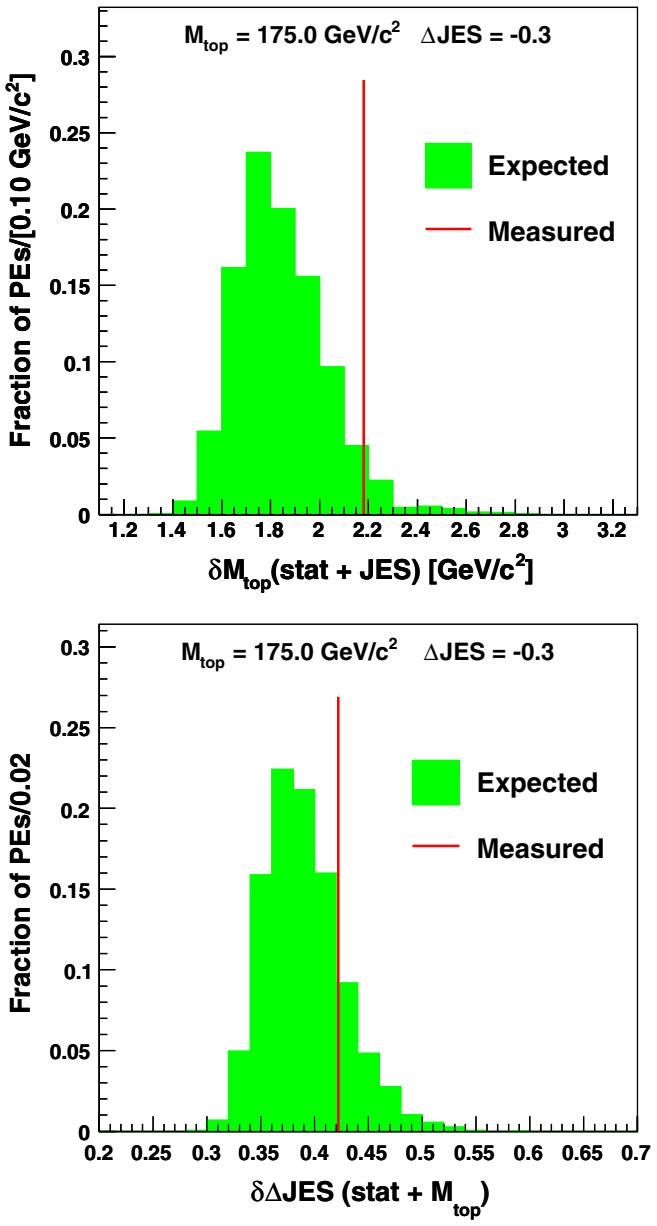

FIG. 11 (color online). Distributions of the uncertainties on the top quark mass (upper plot) and the jet energy scale displacement (lower plot) as expected from default PEs performed using as input values $M_{\rm top}^{\rm in} = 175.0$ GeV$/c^2$ and $\Delta{\rm JES}^{\rm in} = -0.3$. The vertical lines indicate the uncertainties obtained in our reported result.

$$\Delta{\rm JES} = -0.30 \pm 0.47({\rm stat} + M_{\rm top})^{+0.34}_{-0.37}({\rm syst}), \quad (28)$$

which, isolating the purely statistical contributions and adding the uncertainties from JES and $M_{\rm top}$ to the respective systematic uncertainties, can also be written as

$$M_{\rm top} = 174.8 \pm 1.7({\rm stat})^{+2.0}_{-1.9}({\rm syst})\ {\rm GeV}/c^2, \quad (29)$$

$$\Delta{\rm JES} = -0.30 \pm 0.35({\rm stat})^{+0.47}_{-0.49}({\rm syst}). \quad (30)$$

This measurement of the top quark mass has been used in the current world average [5].

XII. CROSS SECTION MEASUREMENT

The procedure used to measure the top quark mass also returns the average number of signal events expected, given the selected data samples. These results can be turned into a measurement of the $t\bar{t}$ cross section, as follows.

A. The likelihood function

From the number of signal events, $n_s^{1\ {\rm tag}}$ and $n_s^{\geq 2\ {\rm tags}}$, as obtained from the mass likelihood fit, we derive a measurement of the $t\bar{t}$ production cross section considering the efficiency for selecting a $t\bar{t}$ event in the two tagging categories.

The cross section measurement is performed by maximizing a likelihood function which can be divided into two parts:

$$\mathcal{L} = \mathcal{L}_{1\ {\rm tag}} \times \mathcal{L}_{\geq 2\ {\rm tags}}, \quad (31)$$

where each term can be expressed as

$$\mathcal{L}_{1,\geq 2\ {\rm tags}} = \mathcal{L}_{\sigma_{t\bar{t}}} \times \mathcal{L}_{\epsilon}, \quad (32)$$

where

$$\mathcal{L}_{\sigma_{t\bar{t}}} = \exp\left[-\frac{(\sigma_{t\bar{t}} \cdot \epsilon \cdot {\rm L} - n_s)^2}{2\sigma_{n_s}^2}\right] \quad (33)$$

contains all the parameters of the fit, i.e. the production cross section $\sigma_{t\bar{t}}$, the integrated luminosity L, the signal efficiency ϵ, and the signal yield $n_s \pm \sigma_{n_s}$, as given by the mass measurement, while $\mathcal{L}_{\epsilon}$ is a Gaussian term constraining the efficiency within its statistical uncertainty.

The efficiencies are evaluated using a sample of about 4×10^6 $t\bar{t}$ events generated with $M_{\rm top} = 175$ GeV$/c^2$ and assuming $\Delta{\rm JES} = -0.3$, i.e. the value we measured by the mass likelihood fit, and are summarized along with signal yields and other parameters in Table VI.

While studying the performance of the procedure, using pseudoexperiments produced assuming a given input cross section, we observe the need to introduce a small correction. The outcome of the fit needs to be multiplied by a factor $k_\sigma = 0.982 \pm 0.008$ in order to obtain an unbiased measurement of the cross section.

From the maximization of the likelihood, we obtain a central value for the $t\bar{t}$ production cross section

$$\sigma_{t\bar{t}} = 7.2 \pm 0.5({\rm stat}) \pm 0.4({\rm lum})\ {\rm pb}, \quad (34)$$

evaluated assuming $M_{\rm top} = 175$ GeV$/c^2$ and $\Delta{\rm JES} = -0.3$, close to the values measured in Sec. XI. The first uncertainty is the statistical one, while the second one derives from the 6% uncertainty on the integrated lumi-

TABLE VI. Input variables to the cross section evaluation. For the signal yields, the first uncertainty is the purely statistical one.

Variable	Input value
Signal yield, one tag	$643 \pm 59 \pm 54$
Signal yield, ≥ 2 tags	$216 \pm 21 \pm 14$
Efficiency, one tag	$(3.55 \pm 0.01)\%$
Efficiency, ≥ 2 tags	$(1.00 \pm 0.01)\%$
Integrated luminosity	2874 ± 172 pb^{-1}

TABLE VII. Cross section as evaluated assuming different values for M_{top} and ΔJES.

M_{top} (GeV/c^2)	ΔJES	$\sigma_{t\bar{t}}$ (pb)
175.0	-0.3	7.24
175.0	0.0	7.00
172.5	0.0	7.21
170.0	0.0	7.29

nosity. As the signal efficiencies depend strongly on the assumed values for M_{top} and ΔJES, the measured $t\bar{t}$ cross section also has the same dependence. For reference we report in Table VII the cross sections corresponding to other (M_{top}, ΔJES) points with a top quark mass near the current CDF average. In this case we assume $\Delta\text{JES} = 0$, and the systematic uncertainty on JES is increased from 6.1% to 9.2%, corresponding to changing the ΔJES by ± 1 rather than by ± 0.6 units, that is, the sum in quadrature of the uncertainties on the measured jet energy scale, Sec. XI.

B. Systematic uncertainties

Most of the sources of systematic uncertainties affecting the measurement of $\sigma_{t\bar{t}}$ are the same as the ones discussed for the measurement of the top quark mass. We just need to evaluate their effects both on the signal yields and on the signal efficiencies in order to derive the effects on the cross section. There are few other sources of systematic uncertainty specific to a cross section measurement which have not been discussed in Sec. X, because they affect only the signal efficiencies. These include the uncertainty on the calibration constant, k_σ, on the $W \rightarrow$ hadrons branching ratio (BR) [24], on the trigger simulation, and on the distribution of the primary vertex z coordinate. As for the effect of the JES uncertainty on the efficiency, we have evaluated it by changing the ΔJES by ± 0.6 units with respect to the measured value $\Delta\text{JES} = -0.3$. Residual effects due to individual levels of corrections have been accounted for, too. The relative uncertainties $\Delta\sigma_{t\bar{t}}/\sigma_{t\bar{t}}$ for the individual sources are summarized in Table VIII. Considering their sum in quadrature, the $t\bar{t}$ production cross section amounts to

$$\sigma_{t\bar{t}} = 7.2 \pm 0.5(\text{stat}) \pm 1.0(\text{syst}) \pm 0.4(\text{lum})\ \text{pb}, \quad (35)$$

assuming $M_{\text{top}} = 175\ \text{GeV}/c^2$ and $\Delta\text{JES} = -0.3$.

TABLE VIII. Systematic uncertainties and their relative sizes for the cross section measurement. The total uncertainty is obtained by the sum in quadrature of single contributions.

Source	$\Delta\sigma_{t\bar{t}}/\sigma_{t\bar{t}}$ (%)
Calibration factor	0.8
Generator	4.2
ISR/FSR	0.6
b-jet energy scale	2.8
b-tag SF E_T dependence	5.4
PDF	3.4
Multiple $p\bar{p}$ interactions	2.5
Color reconnection	0.8
Templates statistics	0.8
Background shape	0.3
Background normalization	8.2
JES	6.1
Residual JES	2.1
Primary vertex	0.2
BR($W \rightarrow$ hadrons)	0.8
Trigger	1.8
Total	13.7

XIII. CONCLUSIONS

Using a very effective neural-network-based kinematical selection and a b-jet identification technique, we measure the top quark mass to be

$$M_{\text{top}} = 174.8 \pm 2.4(\text{stat} + \text{JES})^{+1.2}_{-1.0}(\text{syst})\ \text{GeV}/c^2, \quad (36)$$

and the $t\bar{t}$ production cross section to be

$$\sigma_{t\bar{t}} = 7.2 \pm 0.5(\text{stat}) \pm 1.0(\text{syst}) \pm 0.4(\text{lum})\ \text{pb}. \quad (37)$$

These values represent the most precise measurements to date of M_{top} and $\sigma_{t\bar{t}}$ in the all-hadronic decay channel. The results are consistent with the measurements obtained in other decay channels by CDF and D0 Collaborations [5,6] and, as it concerns $\sigma_{t\bar{t}}$, with the theoretical predictions evaluated at the value of the top quark mass obtained in our measurement [3].

ACKNOWLEDGMENTS

We thank the Fermilab staff and the technical staffs of the participating institutions for their vital contributions. This work was supported by the U.S. Department of Energy and National Science Foundation; the Italian Istituto Nazionale di Fisica Nucleare; the Ministry of Education, Culture, Sports, Science and Technology of Japan; the Natural Sciences and Engineering Research Council of Canada; the National Science Council of the Republic of China; the Swiss National Science Foundation; the A. P. Sloan Foundation; the Bundesministerium für Bildung und Forschung, Germany; the World Class University Program, the National Research Foundation of Korea; the Science and

Technology Facilities Council and the Royal Society, United Kingdom; the Institut National de Physique Nucleaire et Physique des Particules/CNRS; the Russian Foundation for Basic Research; the Ministerio de Ciencia e Innovación, and Programa Consolider-Ingenio 2010, Spain; the Slovak R&D Agency; and the Academy of Finland.

[1] S. Heinemeyer *et al.*, J. High Energy Phys. 09 (2003) 075.
[2] LEP Electroweak Working Group, Tevatron Electroweak Working Group, and SLD electroweak and heavy flavour groups, arXiv:0911.2604.
[3] M. Cacciari *et al.*, J. High Energy Phys. 09 (2008) 127; N. Kidonakis and R. Vogt, Phys. Rev. D **78**, 074005 (2008); S. Moch and P. Uwer, Nucl. Phys. B, Proc. Suppl. **183**, 75 (2008).
[4] T. Aaltonen *et al.* (CDF Collaboration), Phys. Rev. D **76**, 072009 (2007).
[5] Tevatron Electroweak Working Group for CDF and D0 Collaborations, arXiv:0903.2503.
[6] T. Aaltonen *et al.* (CDF Collaboration), Phys. Rev. D **79**, 112007 (2009); **79**, 052007 (2009); V. Abazov *et al.* (D0 Collaboration), Phys. Rev. Lett. **100**, 192004 (2008); Phys. Lett. B **679**, 177 (2009).
[7] T. Aaltonen *et al.* (CDF Collaboration), Phys. Rev. D **79**, 072010 (2009); Phys. Rev. Lett. **98**, 142001 (2007).
[8] D. Acosta *et al.* (CDF Collaboration), Phys. Rev. D **71**, 032001 (2005).
[9] L. Balka *et al.*, Nucl. Instrum. Methods Phys. Res., Sect. A **267**, 272 (1988).
[10] M. Albrow *et al.*, Nucl. Instrum. Methods Phys. Res., Sect. A **480**, 524 (2002).
[11] G. Ascoli *et al.*, Nucl. Instrum. Methods Phys. Res., Sect. A **268**, 33 (1988).
[12] D. Acosta *et al.*, Nucl. Instrum. Methods Phys. Res., Sect. A **494**, 57 (2002).
[13] F. Abe *et al.* (CDF Collaboration), Phys. Rev. D **45**, 1448 (1992).
[14] D. Acosta *et al.* (CDF Collaboration), Phys. Rev. D **71**, 052003 (2005).
[15] A. Abulencia *et al.* (CDF Collaboration), Phys. Rev. D **74**, 072006 (2006).
[16] A. Bhatti *et al.*, Nucl. Instrum. Methods Phys. Res., Sect. A **566**, 375 (2006).
[17] The missing transverse energy $\vec{\not\!\!E}_T$ is calculated as the vector sum of the energy in each calorimeter tower multiplied by a unit vector in the azimuthal direction of the tower. If isolated high momentum muons are found in the event, the $\vec{\not\!\!E}_T$ is corrected by subtracting the muon energy in the calorimeter and adding the muon p_T to the vector sum. $\not\!\!E_T$ is defined as the magnitude of $\vec{\not\!\!E}_T$.
[18] D. Acosta *et al.* (CDF Collaboration), Phys. Rev. Lett. **96**, 202002 (2006).
[19] MLPFIT: A Tool for Multi-Layer Perceptrons, http://schwind.home.cern.ch/schwind/MLPfit.html.
[20] R. Brun and F. Rademaker, ROOT Version 4.00/08, http://root.cern.ch/.
[21] T. Sjöstrand *et al.*, Comput. Phys. Commun. **135**, 238 (2001).
[22] A. Abulencia *et al.* (CDF Collaboration), Phys. Rev. D **73**, 032003 (2006).
[23] The $\geq$ 2-tag sample actually consists of events with two or three tagged jets. When three tags are present, the two leading ones are assigned to b quarks.
[24] C. Amsler *et al.* (Particle Data Group), Phys. Lett. B **667**, 1 (2008).
[25] S. M. Oliveira, L. Brucher, R. Santos, and A. Barroso, Phys. Rev. D **64**, 017301 (2001).
[26] G. Marchesini *et al.*, Comput. Phys. Commun. **67**, 465 (1992); G. Corcella *et al.*, J. High Energy Phys. 01 (2001) 010.
[27] H. L. Lai *et al.*, Eur. Phys. J. C **12**, 375 (2000).
[28] A. D. Martin, R. G. Roberts, W. J. Stirling, and R. S. Thorne, Eur. Phys. J. C **4**, 463 (1998).
[29] P. Skands and D. Wicke, arXiv:0807.3248; P. Skands, arXiv:0905.3418.